University of California
Los Angeles

Realistic Simulation and Control of Human Swimming and Underwater Movement

A dissertation submitted in partial satisfaction
of the requirements for the degree
Doctor of Philosophy in Computer Science

by

Weiguang Si

2013

Abstract of the Dissertation

Realistic Simulation and Control of Human Swimming and Underwater Movement

by

Weiguang Si

Doctor of Philosophy in Computer Science

University of California, Los Angeles, 2013

Professor Demetri Terzopoulos, Chair

We present a multiphysics framework for the realistic animation of human swimming that features a comprehensive biomechanical model of the human body immersed in simulated fluid. Our human model includes all of the relevant articular bones and muscles, including 103 bones (comprising 163 articular degrees of freedom) plus a total of 823 muscle actuators embedded in a finite element model of the the soft tissues of the body that produces realistic deformations. A main focus of this thesis is the control of this complex biomechanical model. To coordinate the numerous muscle actuators in order to produce natural swimming movements, we develop a biomimetically motivated motor control system based on Central Pattern Generators (CPG), which learns to produce activation signals that drive the Hill-type muscle actuators. In addition, we introduce an optimization-based control method that enables our human model to achieve non-locomotion, task-oriented movements, such as changing the orientation of the body in the water.

The dissertation of Weiguang Si is approved.

Joseph M. Teran

Song-Chun Zhu

Stanley J. Osher

Demetri Terzopoulos, Committee Chair

University of California, Los Angeles

2013

To my mother, father and brother

Table of Contents

List of Figures

List of Tables

Acknowledgments

My advisor, Professor Demetri Terzopoulos, has been my mentor both in academic research and in life. I was deeply attracted to his fascinating work in computer graphics and computer vision. I was so impressed by his insights into the great challenges and opportunities in advanced computer animation that I decided to pursue my PhD study in this area. It has been a great honor to be his student and a very nice experience to work with him. Demetri encouraged me to set ambitious goals and the highest standards in my work, and he also did a lot to help me realize my career dreams. This thesis would never have materialized without his guidance and support.

I thank Professors Stanley Osher, Song-Chun Zhu, and Joseph Teran for serving on my thesis committee and offering me their advice on how to improve my dissertation.

I acknowledge with particular appreciation the contributions of Professors Sung-Hee Lee and Eftychios Sifakis. Sung-Hee has been my very helpful mentor in multibody dynamics simulation and human motion control, and I learned a lot from him about these topics. The biomechanical human model that I have used in my research is also largely based on the musculoskeletal human body model that he developed in his UCLA PhD thesis. I had a chance to visit his lab and work closely with him while he was a professor at the Gwangju Institute of Science and Technology in Korea and I thank him very much for his generous support during my visit. Eftychios has also been a great mentor in physics-based simulation, and he taught me a lot about fluid simulation and deformable solid simulation. The work on simulating soft tissues reported in this thesis is primarily his. I am deeply grateful for the collaboration of Sung-Hee and Eftychios.

My appreciation also goes to my wonderful colleagues. I would like to express my gratitude to Wenjia Huang, Craig Yu, Kresimir Petrinec, Gabriele Nataneli,

Shawn Singh, Mubbasir Kapadia, Brian Allen, Billy Hewlett, Gautam Prasad, Masaki Nakada, Eduardo Poyart, Konstantinos Sideris, Matthew Wang, Gergely Klar, Sharath Gopal, Chenfanfu Jiang, Jingyi Fang, Xiaowei Ding, Xiaolong Jiang, Alexey Stomakhin, Garett Ridge, Joyce Kuo, Wilson Yan for sharing their knowledge and ideas with me and for making our lab a great place in which to work.

I thank Dr. Alex Vasilescu for supervising me in the IARPA-funded face recognition project that provided RA support to me over a 2-year period. I am grateful to Brain Guenter, Michael Jones, Rachel Rose, Zoran Kacic-Alesic, Chris Twigg and Yuting Ye for mentoring me during my internships at Microsoft Research, Mitsubishi Electric Research Laboratories, and Industrial Light & Magic, and also thank them for their great influence in my career development.

My parents spared no sacrifice to nurture me and avail me of the best possible education. I thank them for their support and unconditional love. I would also like to thank my brother for accompanying our parents while I was unable to be with them. I am deeply grateful to my family for making all of this possible.

Vita

2008	B.E., Electronic Engineering Tsinghua University Beijing, China.
2009–2010	Research Assistant Computer Science Department University of California, Los Angeles Los Angeles, California
2011	Teaching Assistant Computer Science Department University of California, Los Angeles Los Angeles, California
2012	Visiting Researcher University of Wisconsin-Madison Madison, WI
2012	Visiting Researcher Gwangju Institute of Science and Technology Gwangju, Korea
2009	Research Intern Microsoft Research Redmond, WA
2010	Research Intern Mitsubishi Electric Research Laboratories Cambridge, MA

2011	R&D Intern
	Industrial Light & Magic, Lucasfilm Ltd.
	San Francisco, CA
2012	R&D Intern
	Industrial Light & Magic, Lucasfilm Ltd.
	San Francisco, CA

Publications

W. Si and B.K. Guenter (2010). "Linear-Time Dynamics for Multibody Systems with General Joint Models." *ACM SIGGRAPH/Eurographics Symposium on Computer Animation (SCA)*, Madrid, Spain, July, 2010, 31–38.

W. Si, S.-H. Lee, E. Sifakis, D. Terzopoulos (2014). Realistic Simulation and Control of Human Swimming. *ACM Transactions on Graphics* (provisionally accepted for publication; in revision).

CHAPTER 1

Introduction

The simulation of human motion is of great interest in computer graphics, robotics, biomechanics, control theory, and other disciplines. Among the many approaches proposed to synthesize human movement, efforts that involve modeling the detailed anatomical structure and biomechanical characteristics of the human body, in conjunction with the design of motion controllers ideally capable of adapting to the body's environment, have progressed steadily. Despite the progress, it remains a grand challenge to achieve anatomically detailed simulation of human motion with impeccable realism.

To synthesize realistic, anatomically detailed human animations in a physics-based manner, we must construct a comprehensive human model with synthetic hard (bone) and soft (flesh) tissues properly coupled and simulated, and we must also design sophisticated motor controllers for this biomechanical model that can produce natural human motions. In our work, we are especially interested in aquatic environments for several reasons. On the one hand, the dynamically rich physical interaction of the human body with water provides a fertile proving ground that confronts a biomechanical human simulation/control system with fascinating and difficult motor control problems. On the other hand, the aquatic environment is somewhat forgiving in that it provides a stabilizing effect, which leads to nonetheless interesting control scenarios that serve as good starting points for designing more sophisticated human motor controllers suitable for terrestrial environments. There are many elegant human motions possible in the aquatic

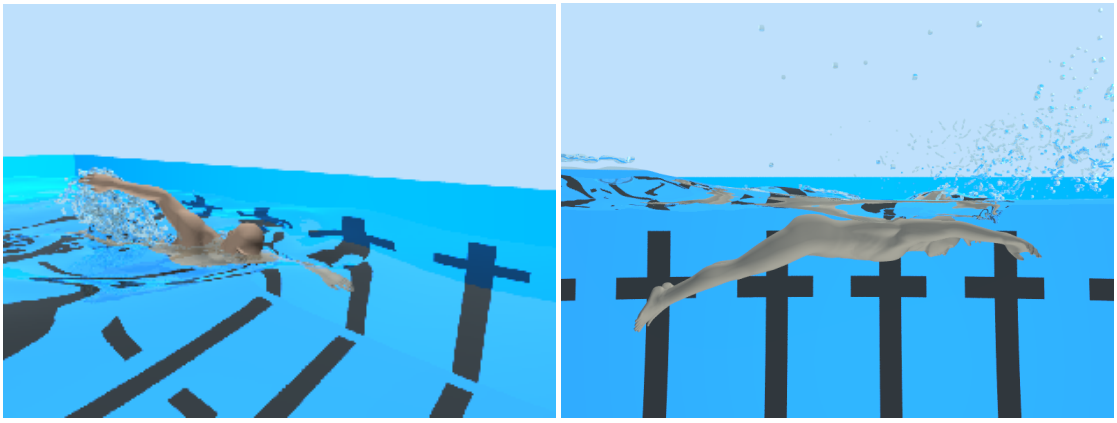

Figure 1.1: Realistic simulation and control of human swimming. The autonomously controlled biomechanical model simulates swimming in crawl (left) and butterfly (right) strokes.

environment that deserve study from the perspective of simulation and control, such as swimming for locomotion, artistic synchronized swimming, water polo, diving, etc.

1.1 Multiphysics Simulation Framework

In this thesis, we develop a sophisticated multiphysics simulation framework for human swimming within which we successfully develop several musculoskeletal controllers for realistically synthesizing various human motions in water (Figure 1.1). Our simulation framework for realistic human swimming comprises three mutually coupled specialized component simulators—an articulated multibody simulator for the muscle-actuated skeleton, a (Lagrangian) deformable solid simulator for the flesh, and a (Eulerian) fluid simulator for the water.

Our biomechanical human model (Figure 1.2) includes all of the relevant articular bones and muscles, including 103 rigid bones plus a total of 823 Hill-type muscles modeled as piecewise line segment (PLS) contractile actuators, and we take advantage of the anatomically appropriate muscle actuator redundancy to

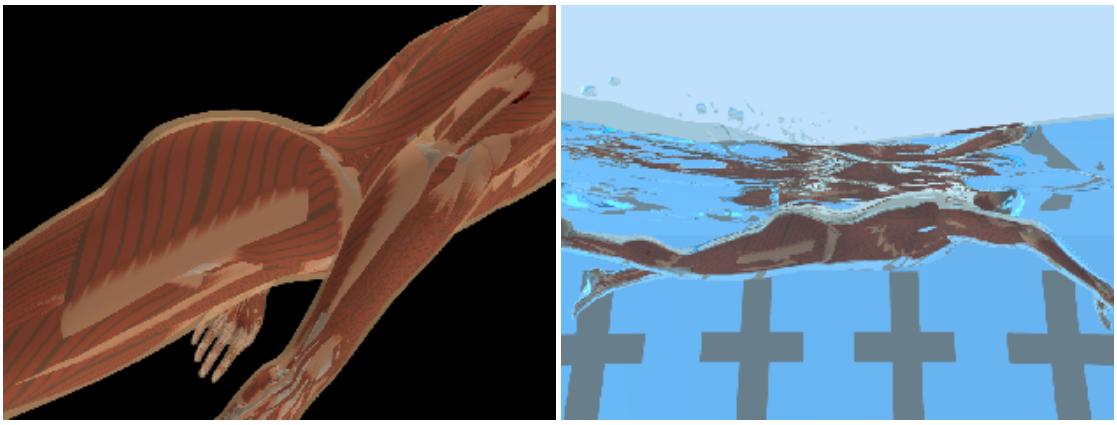

Figure 1.2: Left: A closeup view of the biomechanical human model rendered with transparent skin to reveal the muscle geometries. Right: The biomechanical model immersed in simulated water.

achieve robust motor control. A muscle-actuated articulated skeleton simulation synthesizes detailed biomimetic motions of the rigid bones in conjunction with a deformable soft tissue simulation that synthesizes muscle-driven dynamic deformations of the flesh using lattice-based discretization of quasi-incompressible elasticity augmented with active contractile muscle terms. To simulate the water environment in which the biomechanically simulated body floats, we employ an Eulerian (Navier-Stokes) fluid simulation on a MAC grid and use a particle level set method to track the surface of the water.

We simulate the coupling between the bone and flesh as well as the coupling between the flesh and water in an interleaved manner. This approach has several advantages over a tight two-way coupling. Tightly coupling the articulated rigid bodies, deformable solid, and surrounding fluid would be challenging and computationally expensive. Interleaved coupling makes our simulation framework much more flexible and it allows for the reuse and improvement of the individual simulation components.

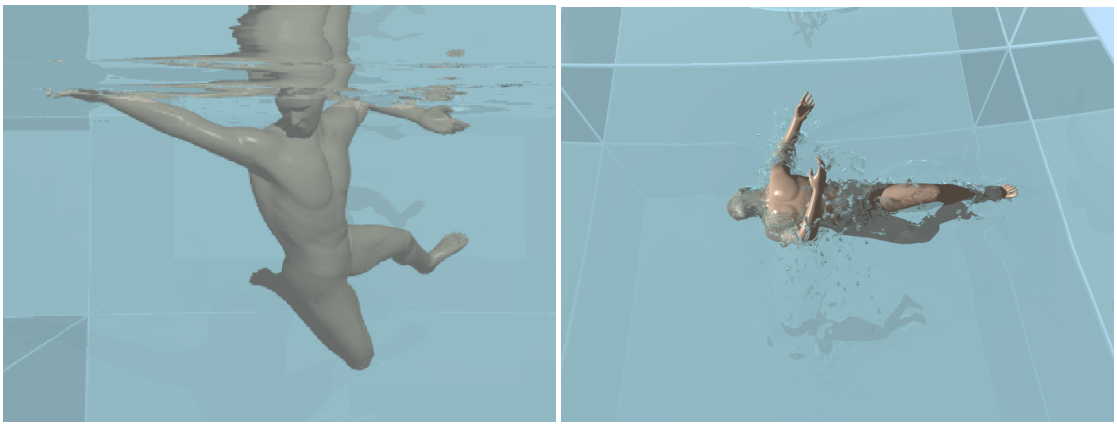

Figure 1.3: Control of body orientation in the water

1.2 Controlling the Biomechanical Human Model

In addition to the multiphysics framework for simulating realistic human swimming with a comprehensive biomechanical model, our work makes a number of additional contributions. We are primarily concerned with the control aspects of the biomechanical human model within our multiphysics simulation framework. In particular, we develop two different types of motor controllers—a *locomotion controller* that produces realistic swimming (Fig. 1.1) and a *task-oriented controller* for natural orientation control of the swimmer's body (Fig. 1.3). The two types of controllers represent different successful approaches to controlling the numerous muscle actuators in order to synthesize, respectively, repetitive and non-repetitive natural body motions in the simulated fluid environment.

CPG Locomotion Control: For locomotion control, we develop a biomimetic motor control system based on *Central Pattern Generators (CPGs)*, which produces activation signals that drive the many Hill-type muscle actuators. CPGs are neural networks that are capable of generating coordinated patterns of rhythmic activity without input from higher motor control centers in the brain. They offer advantages that are desirable in addressing biomechanical control problems.

First, CPG models typically have just a few control parameters that modulate the locomotion pattern. Thus, a properly implemented CPG model reduces the dimensionality of the low-level motor control problem such that higher-level controllers need only generate task-oriented control signals. This is one of the most interesting features of biological CPGs. Second, CPG models typically produce smooth modulations of the controlled trajectories, even when the control parameters are changed abruptly. Third, CPGs produce stable rhythmic patterns, which enable the system to rapidly return to its normal rhythmic behavior after transient perturbations of the state variables. We create a CPG muscle controller that produces appropriate muscle contraction forces in the virtual swimmer's body, which induce the human model to perform various swimming motions. The CPG networks are divided into 10 groups to control different parts of the body. Each CPG group comprises a number of CPG units, one unit per muscle. Each CPG unit, which is associated with a single muscle, is modeled as a nonlinear dynamical oscillator that can guarantee basic stability and convergence properties of the learned control signal. Our CPG controller can generate muscle contraction signals to produce various swimming motions by simply varying a few parameters, and it is robust against external perturbations.

Multiobjective Task-Oriented Control: The CPG-based approach is inappropriate for motor control scenarios in which the required muscle contraction signals are aperiodic. Thus, for non-locomotive, task-oriented control, we develop a novel multiobjective control strategy that enables the biomechanical human model to achieve the task naturally. Our method tackles the task-oriented control problem in joint space using a multiobjective optimization approach, and then it computes the muscle control signals needed to generate the desired joint torques. The objective function takes into account three factors—task accomplishment, motion naturalness, and self-collision avoidance. A new feature of this control

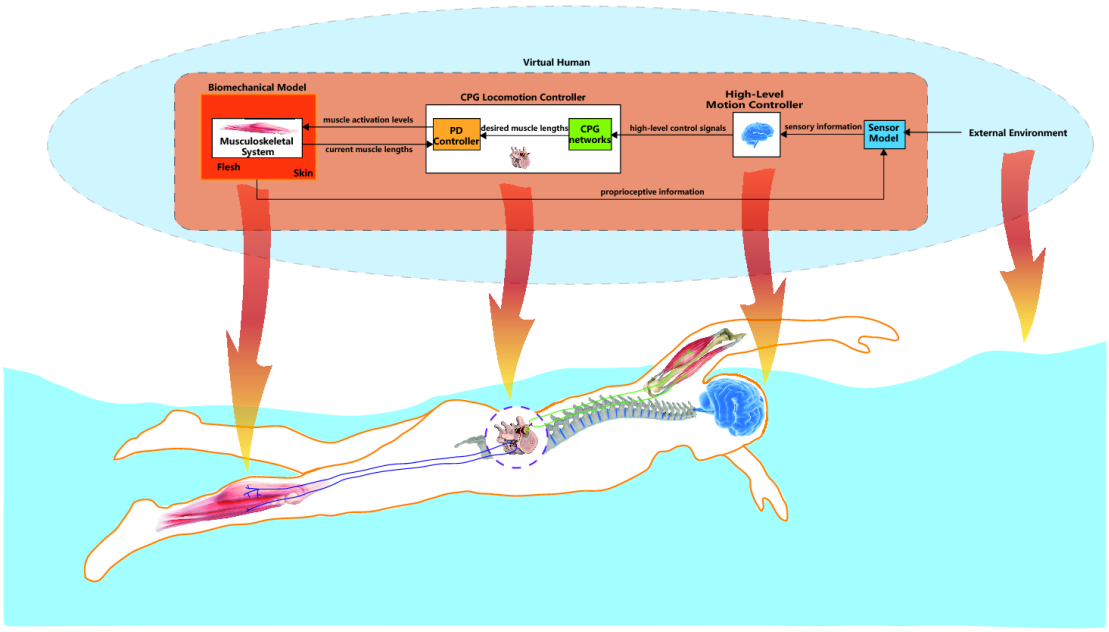

Figure 1.4: Overview of our biomimetic human swimming simulation and control framework.

method is that the physics-based task objective, which is formulated using physical laws within a multibody dynamics framework with self collision avoidance handled as soft constraints, is augmented by a statistical component, a Gaussian Process Dynamical Model (GPDM) that enhances the naturalness of the motion. We apply our approach to create an orientation controller that enables the biomechanical human model to control its orientation naturally in the water.

1.3 Overview

Figure 1.4 illustrates the overall biomimetic structure of our human swimming simulation and control framework. Our autonomous virtual human comprises the biomechanical body model with its skeletal, active muscular, and passive soft-tissue components, and a brain model with a perception center that encompasses proprioception as well as the sensing of visual targets in the environment. The

motor center of the brain has a low-level CPG locomotion controller (emulating biological CPG networks in the spinal cord) and one that produces higher-level motor signals such as swimming style, speed, turn direction/sharpness, etc., taking the perceptual information into account. Given these motor signals as inputs, the CPG networks automatically synthesize the desired muscle length signals online, from which a proportional/derivative (PD) control mechanism produces the associated activation levels that innervate the muscles whose contractions actuate the biomechanical body. Our multiphysics simulation framework simulates the biomechanical human model along with the aquatic environment in which it is situated, as well as their physical interaction.

The remainder of this thesis is organized as follows: Chapter 2 reviews relevant prior research in the graphics, robotics, and biomechanics literature. Chapter 3 presents our multiphysics simulation framework, detailing all the simulation components and how they are coupled in our system. The primary focal points of this thesis are our CPG-based locomotion control and task-oriented control through multiobjective optimization, which work within our simulation framework to produce natural swimming and aquatic motions; Chapter 4 develops our locomotion controller and Chapter 5 develops our task-oriented controller. Chapter 6 reports our experiment results, which reveal that our complex yet appropriately controlled human model demonstrates coordinated swimming tasks and orientation control tasks. Chapter 7 discusses the benefits and limitations of specific technical choices that we have made in our framework and reports on an additional set of experiments aimed at assessing the importance of various of its simulation/control components relative to alternative approaches. Chapter 8 presents conclusions and proposes avenues for future work.

CHAPTER 2

Related Work

Our work builds upon relevant technical advances in computer graphics, robotics, and biomechanics to model the biomechanical characteristics of human body and emulate its motor control mechanisms, as well as to simulate the continuum mechanics of the relevant solids and fluids.

2.1 Biomechanical Human Modeling

In graphics, researchers have traditionally used joint torques to drive articulated skeletal animation (Hodgins et al., 1995; Faloutsos et al., 2001), in contrast to facial animation where muscle actuators have been used for two decades to synthesize expressions (Waters, 1987; Lee et al., 1995). As a means of improving realism, skeletal muscle driven motion generation is receiving growing attention and researchers have been developing increasingly sophisticated biomechanical models of individual body segments actuated by muscles—e.g., the arm (Albrecht et al., 2003; Tsang et al., 2005; Sueda et al., 2008), leg (Komura et al., 2000; Dong et al., 2002; Wang et al., 2012), neck (Lee and Terzopoulos, 2006), and trunk (Zordan et al., 2006)—and also of the entire body (Nakamura et al., 2005). However, the simulation of deformable flesh to produce a detailed anatomical animation of soft tissue is missing in these previous efforts. The closest precedent to the biomechanical human model that we have developed is the upper-body musculoskeletal model reported in (Lee et al., 2009), which employed a one-way coupling between flesh and bones. Ours is a full-body comprehensive human

model with two-way flesh-bone coupling.

2.2 Underwater Motion Simulation

Early work on simulating the underwater motions of aquatic creatures adopted rather simple solid and fluid models: Tu and Terzopoulos (1994) simulated fishes using a simple biomechanical model, a mass-spring-damper system to model piscine bodies immersed in a simplified fluid model. Yang *et al.* (2004) used an articulated body representation and a simplified fluid model. As the simulation techniques for solids and fluids advance, researchers have used increasingly sophisticated fluid models and solid-fluid coupling techniques for simulating underwater creatures. Kwatra *et al.* (2010) and Tan *et al.* (2011) used a simplified articulated body representation and two-way coupling between the body and a fluid simulation to model creatures locomoting in fluids. Lentine *et al.* (2011) employed articulated skeletons with a deformable skin layer and two-way coupling to a fluid simulator to model figures moving in fluids. We too employ an articulated (human) skeleton, but also include non-rigid simulated flesh, and use two-way coupling between the deformable skin and water to synthesize natural human aquatic motion.

2.3 Underwater Motion Control

Motion control in underwater creatures was pioneered by Tu and Terzopoulos (1994). Grzeszczuk and Terzopoulos (1995) achieved optimal parameters for underwater gait behavior in rather simple creatures through spatial-temporal optimization methods. Tan *et al.* (2011) proposed a Covariance Matrix Adaptation based optimization to create realistic swimming behavior for a given articulated creature body. However, achieving sophisticated human swimming styles through spatial-temporal optimization is a huge challenge as one must define a tailored

objective function for each style. Other methods have therefore been developed to create gait motions for more complex systems such as humans. Yang *et al.* (2004) developed a layered strategy for human swimming control in which each control layer is procedurally modeled and empirically tuned to create physics-based swimming motion in real time. Kwatra *et al.* (2010) developed a swimming controller that computes the necessary joint torques to follow captured human motions that mimic swimming.

We develop a CPG-based locomotion controller that, after learning a few CPG parameters, automatically generates muscle contraction signals that enable the human model to perform swimming motions. Our controller is robust against external perturbations and is furthermore able to achieve more complex tasks, such as changing speed, turning, swimming style transition, etc. CPGs are neural circuits found in both invertebrate and vertebrate animals that can produce rhythmic patterns of neural activity without receiving rhythmic inputs. Research in biology and robotics has shown that animal locomotion is in large part based on CPGs (MacKay-Lyons, 2002; Ijspeert, 2008). CPG models have already been successfully applied to robotic control. Ijspeert *et al.* (2007) built an amphibious salamander robot controlled by CPG models and developed in (Righetti and Ijspeert, 2006) a programmable CPG for the online generation of periodic signals to control bipedal locomotion in a simulated robot. Taga (1995) constructed a human locomotion controller based on CPGs and Hase *et al.* (2003) optimized this controller for 3D musculoskeletal models without activation dynamics. The aforementioned efforts employ CPGs to generate desired joint angle signals, whereas we use CPGs to generate the desired muscle lengths. Muscle length control has several advantages over joint angle control in our case, among them easy computation of the activation levels needed to drive the contractile muscle actuators using a simple feedback scheme, which makes it very suitable to control our biomechanical human model.

For non-locomotive tasks, global spacetime optimization will be almost impos-

sible in our case; as we explain in Chapter 5, local optimization is more practical. Lentine *et al.* (2011) treated motion control as an optimization problem where rather simple creatures move by locally seeking solutions to objective functions. Their controllers are tightly interactive to the surrounding fluid and show interesting creature movement by minimizing or maximizing drag and lift. Our task-oriented controller is also based on local optimization in time. Our multiobjective strategy achieves natural underwater motions by augmenting the physics-based task objective with a data-driven naturalness objective.

Physics-based simulation can generate physically plausible human motions, but physical laws alone are insufficient to generate natural human motions, since such motions can be physically correct yet appear unnatural. One way to address this problem is to apply optimization strategies. Witkin and Kass (1988) postulated that a physically-simulated character should minimize its effort to synthesize a movement subject to certain constraints (see also (Grzeszczuk and Terzopoulos, 1995)). Numerous performance criteria for human motion modeling, e.g. minimal energy, minimal torque variation, minimal jerk, etc., have been introduced by computer animation researchers. However, to apply these performance criteria, we generally must perform non-convex global optimization over a time interval, which is very expensive for our case, as we discuss in Chapter 5.

Statistical approaches provide another way to get natural motion. Gaussian Processes (GPs) and their variants (e.g., GPLVM (Lawrence, 2004), GPDM) have recently attracted interest in computer animation for creating natural kinematic motion, including inverse kinematics (Grochow et al., 2004), motion interpolation (Mukai and Kuriyama, 2005), motion editing (Ikemoto et al., 2009), and motion synthesis (Ye and Liu, 2010; Wei et al., 2011; Levine et al., 2012). While GP-based methods are able to create natural kinematic human motions, they cannot be directly used in physics-based controllers because, as with other data-driven methods, the resulting motions may be physically infeasible. Wei *et al.* (2011)

proposed an approach to generate physically realistic animations that react to perturbations by learning a nonlinear probabilistic force field function from pre-recorded motion data using GP and combining it with physical constraints in a probabilistic framework. Their approach is effective when the external forces are close to those in the prerecorded motions, but it is unclear whether GP-based methods can reliably model the external forces needed to generate motions that are physically highly dependent on a dynamic fluid environment. Therefore, our approach relies mainly on a physics-based control term to achieve the goal while enhancing the naturalness of the motion using a GPDM, thereby achieving a balance between physical realism and data-driven naturalness.

CHAPTER 3

Simulation and Coupling

In this chapter, we present our multiphysics simulation framework and detail how each of its component simulators serves to animate swimming and underwater motions using a sophisticated biomechanical human model.

3.1 Overview

Our multiphysics simulation framework for realistic human swimming comprises three mutually coupled specialized component simulators—an articulated multibody simulator for the muscle-actuated skeleton, a (Lagrangian) deformable body simulator for the flesh and muscles, and a (Eulerian) fluid simulator for the water. Figure 3.1 illustrates the different simulation components of our multiphysics simulation framework. Figure 3.2 illustrates the different simulation layers of our biomechanical human model.

3.2 Biomechanical Human Simulation Components

We have developed a comprehensive biomechanical human model with 103 rigid bones (comprising 163 articular degrees of freedom) (Figure 3.2(a)), including the vertebrae and ribs, which is actuated by 823 muscles modeled as piecewise uniaxial Hill-type contractile actuators (Figure 3.2(b)). The skeleton is simulated as an articulated, multibody dynamical system. The 3D muscle and passive flesh simulation is accomplished by deforming a lattice-based discretization of

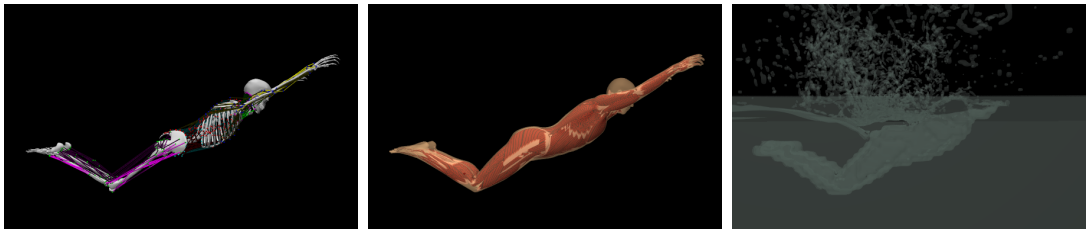

(a) Articulated multibody muscle-actuated skeleton simulation

(b) Lagrangian deformable soft-tissue simulation

(c) Eulerian fluid simulation

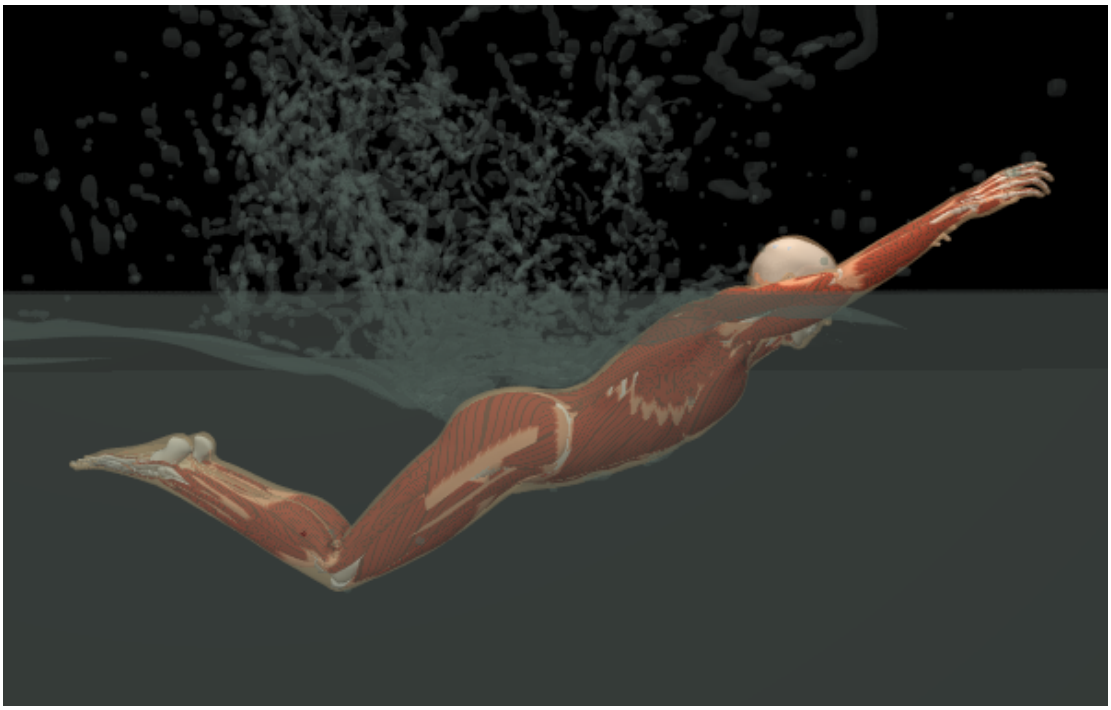

(e) Comprehensive biomechanical swimming simulation

Figure 3.1: Simulation components

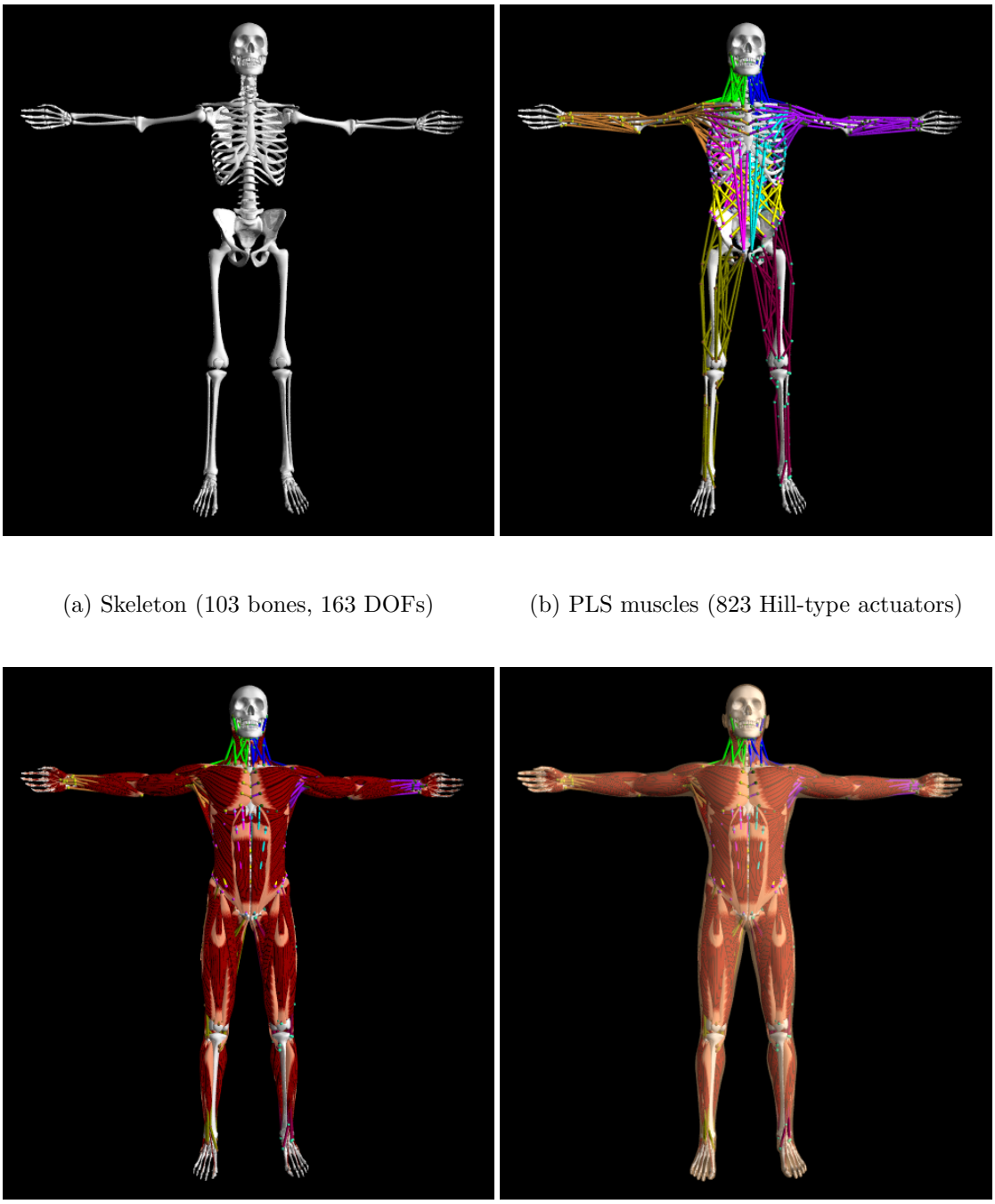

(a) Skeleton (103 bones, 163 DOFs)

(b) PLS muscles (823 Hill-type actuators)

(c) Deforming flesh and muscles

(d) Embedded skin surface

Figure 3.2: Biomechanical human modeling layers

quasi-incompressible elastic material augmented with active muscle terms (Figure 3.2(c)). The inertial properties of the skeleton are approximated from the dense volumetric physical parameters of the soft-tissue elements—each bone's inertial tensor is augmented by the inertial parameters of its associated soft tissues. The natural dynamics of the simulated human are induced by muscle forces generated by the contractile actuators.

The low-level motor control inputs of our biomechanical human model comprise the activation levels of each muscle actuator in the simulated body. The activated muscles generate forces that drive the skeletal simulation. Given the contractile muscle forces, plus the external forces from the flesh simulation, we simulate the skeleton using the Articulated Body Method (Featherstone, 1987) to compute the forward dynamics in conjunction with a backward Euler time-integration scheme as in (Lee et al., 2009). For the purpose of simulating the dynamic deformation of the flesh and muscles, we employ a lattice-based discretization of quasi-incompressible elasticity augmented with active muscle terms. This approach avoids the need for multiple meshes conforming to individual muscles and its regular structure offers significant opportunities for performance optimizations.

3.2.1 Muscle-Actuated Skeleton Simulation

The force generating characteristic of the piecewise uniaxial contractile muscle is governed by a linearized Hill-type model (Lee et al., 2009). Assuming that the length of the tendon is constant, we model a muscle force as the sum of forces from a contractile element (CE), which represents the active muscle force that is controlled by the motor neurons, and a parallel element (PE), which accounts for the passive elasticity of the muscle (Fung, 1993).

The passive elasticity PE force is modeled as a unidirectional exponential

spring:

$$f_P = \max\left(0, k_s\left(\exp(k_c e) - 1\right) + k_d \dot{e}\right), \tag{3.1}$$

where k_s, k_c, and k_d are elastic and damping coefficients, $e = (l - l_0)/l_0$ is the strain of the muscle, with l and l_0 its length and slack length, respectively, and $\dot{e} = \dot{l}/l_0$ is the strain rate.

The CE represents the active muscle force controlled by the motor neurons as

$$f_C = aF_l(l)F_v(\dot{l}), \tag{3.2}$$

where $0 \leq a \leq 1$ is the activation level of the muscle. Force f_C depends on the length and velocity of a muscle. The force-length relation is modeled as $F_l(l) = \max(0, k_{\max}(l - l_m))$, where $k_{\max}$ is the maximum stiffness of a fully activated muscle and l_m is the minimum length at which the muscle can produce force. The force-velocity relation is modeled as $F_v(\dot{l}) = \max(0, 1 + \min(\dot{l}, 0)/v_m)$, where $v_m(\geq 0)$ is the maximum contraction velocity under no load. The control input to the skeleton simulation is the activation level a of each muscle. Chapters 4 and 5 present how our motor controllers determine these muscle activation levels.

Given the muscle forces and other external forces (e.g., gravity.), we perform the simulation of the skeleton using the Articulated Body Method (Featherstone, 1987) for solving the forward dynamics and the backward Euler time-integration scheme.

3.2.2 Soft-Tissue Simulation

The elastic flesh and musculature serves as an intermediary between the fluid environment and the articulated skeleton. The shape and deformation of the flesh volume is determined by the dynamics of the articulated skeleton and the hydrodynamic forces acting on the flesh. Naturally, the exact tissue behavior is also dependent on the geometric layout and material properties of the heterogeneous array of tissue components that constitute the flesh. Some of these material

traits are encoded as static distributions of scalar (e.g., elastic moduli) or vector (e.g., muscle fiber orientation) quantities; other material properties, such as the muscle activations, are time-varying signals that are provided as input to the flesh simulation along with the skeletal dynamics.

We capture the physical behavior of the human swimmer's soft tissue and musculature via numerical simulation of a discrete volumetric model. In designing this discrete representation, we commit to certain simplifying assumptions and modeling approximations to strike a reasonable balance between computational complexity, geometric resolution, biomechanical accuracy and robustness of simulation. First, we do not separately model the skin as a distinct simulation component; for the purposes of fluid-flesh interaction, the contact surface is simply the boundary of the flesh volume and not a separate two-dimensional skin layer. The entirety of the space between the skin and bones is modeled as an elastic continuum; no air-filled cavities or fluid volumes are explicitly simulated as such, although we are free to modulate the elastic properties (e.g., stiffness or compressibility) of such areas to reflect their macroscopic behavior. In addition, the entire flesh volume is assumed to deform as a connected continuum; that is, we do not allow slip or separation in the interior of the flesh volume. Note that connective tissue typically limits the extent of such motions, but there are parts of anatomy where true sliding or separation is possible in the real human body.

For the purpose of simulating the dynamic deformation of flesh and muscle, we employ a lattice-based discretization of quasi-incompressible elasticity augmented with active (contractile) muscle terms. The lattice-based representation (in essence, a lattice deformer) captures the shape of the deforming flesh volume. This discrete model is simply created by superimposing a cubic lattice (we use a lattice size of 10 mm) on a three-dimensional model of the human body, and we discard all cells that do not intersect the flesh volume (i.e., cells that are outside the body, or wholly within solid bones). Of course, the lattice representation thus

created does not accurately capture the geometry of the flesh volume, but provides only a "cubed" approximation. Despite this, we construct the discrete governing equations so as to compensate for this geometric discrepancy. We discretize the equations of elasticity following the methodology of (Patterson et al., 2012), which captures the fact that lattice elements on the boundary of the flesh volume are only fractionally covered by elastic material. The jagged boundary of the lattice-derived simulation volume also differs from the actual skin surface where fluid forces are to be applied; we compensate for that by embedding a high-resolution skin surface mesh within the cubic lattice (Figure 3.2(d)) and distributing the forces acting on the skin surface into the volumetric lattice by scaling with the appropriate embedding weights as discussed in (Zhu et al., 2010). Finally, since the contact surface between the flesh and bones is not resolved in the lattice-derived mesh, we use stiff zero-rest-length springs to elastically attach points sampled on bone surfaces to embedded locations in the flesh simulation lattice, as detailed by (Lee et al., 2009; McAdams et al., 2011).

3.2.2.1 Flesh Constitutive Model

The deformable collection of flesh, skin, and muscle are modeled as a hyperelastic solid. The elastic energy associated with it is partitioned as follows:

$$E_{\text{total}} = E_{\text{iso}} + E_{\text{muscle}} + E_{\text{vol}} + E_{\text{att}}. \tag{3.3}$$

In this expression, $E_{\text{iso}} = \int_{\Omega} \Psi_{\text{iso}}(\mathbf{F}) d\mathbf{X}$ is a strain energy of an isotropic "foundation" material which corresponds to passive flesh (predominantly fatty tissue), where $\mathbf{F} = \partial\phi/\partial\mathbf{X}$ denotes the deformation gradient of the 3D deformation function $\phi : \Omega \to \mathbf{R}^3$, which maps material coordinates $\mathbf{X}$ to world-space deformed locations $\mathbf{x} = \phi(\mathbf{X})$. For the subset Ω_m of the body, which is covered by muscle, an additional anisotropic energy term $E_{\text{muscle}} = \int_{\Omega_m} \Psi_{\text{muscle}}(\mathbf{F}) d\mathbf{X}$ is added, to account for the directional passive/active response of fibrous muscle tissue. The

energy term E_{vol} enforces volume preservation in the flesh. Finally, the energy term E_{att} is associated with the elastic attachment constraints that couple the flesh and bone.

The isotropic component of the strain energy density is formulated as a Mooney-Rivlin material

$$\Psi_{\text{iso}}(\mathbf{F}) = \mu_{10}(\|\mathbf{F}\|_F^2 - 3) + \frac{\mu_{01}}{2}(\|\mathbf{F}\|_F^4 - \|\mathbf{F}^T\mathbf{F}\|_F^2 - 6) \tag{3.4}$$

with parameter values $\mu_{10} = 20$ KPa, $\mu_{01} = 60$ KPa. Note that we use a simple, non-deviatoric formulation of Mooney-Rivlin hyperelasticity. Our formulation supports strong incompressibility; thus, factoring out the hydrostatic stress component is not essential ($\mathbf{F}$ will be forced to have unit determinant by means of the strong incompressibility penalty). The anisotropic component of the strain energy is expressed as:

$$\Psi_{\text{muscle}} = \sum_k \Psi_m^{(k)}(\mathbf{F}; \mathbf{w}_k; a_k)\,[\mathbf{X} \text{ covered by muscle } k], \tag{3.5}$$

where $\mathbf{w}_k$ and a_k are the fiber direction and activation level of the k-th muscle, respectively. The energy density term associated with the k-th muscle is a function $\Psi_m^{(k)}(\lambda_k, a_k)$ of the along-fiber stretch ratio $\lambda_k = \|\mathbf{F}\mathbf{w}_k\|_2$ and the respective activation value a_k. Quantity $\Psi_m^{(k)}$ is defined indirectly through its derivative with respect to λ_k; in fact, $\partial\Psi_m^{(k)}/\partial\lambda_k = T(\lambda_k, a_k)$ is the directional tension function resulting from the sum of the passive elasticity and force-length terms used in the muscle-actuated skeleton simulation. The strain rate and force-velocity terms have been omitted for simplicity, a decision further motivated by the fact that we use a non-validated generic Rayleigh damping model for the isotropic flesh, which would dilute the accuracy of an elaborate force-velocity formulation.

3.2.2.2 Incompressibility

We enforce volume preservation in the elastic material via a penalty term $E_{\text{vol}} = \int_\Omega \Psi_{\text{vol}}(J)d\mathbf{X}$, where $\Psi_{\text{vol}}(J) = \kappa \log^2(J)/2$, with $J = \det \mathbf{F}$, is the volume

change ratio, and the bulk modulus κ is set to 20 MPa. In order to improve the numerical conditioning of this quasi-incompressible material, we transition to a mixed displacement/pressure energy formulation:

$$\hat{E}(\mathbf{x}, p) = E_{\text{att}} + \int_{\Omega} \left[\Psi_{\text{iso}}(\mathbf{F}) + \Psi_{\text{muscle}}(\mathbf{F}) + \alpha p \log(J) - \frac{\alpha^2 p^2}{2\kappa} \right] d\mathbf{X}. \quad (3.6)$$

As is known from the theory of mixed discretizations, the spatial gradients $\mathbf{f} = -\partial E/\partial \mathbf{x}$ and $\hat{\mathbf{f}} = -\partial \hat{E}/\partial \mathbf{x}$ of the two energy formulas (corresponding to elastic forces) are *equal* when the mixed energy $\hat{E}$ is stationary with respect to a variation in the pressure field. Thus, we construct a time-integration scheme by computing forces according to $\hat{\mathbf{f}}(\mathbf{x}, p) = -\partial \hat{E}(\mathbf{x}, p)/\partial \mathbf{x}$, and append the stationarity condition $\partial \hat{E}/\partial p = 0$ to the time integration equations. The result obtained is the same as the pure-displacement formulation, but the discrete equations remain well conditioned regardless of the degree of incompressibility. The price we pay for this favorable conditioning is that the discrete time integration equations become symmetric indefinite, thus a Krylov solver such as MINRES, SYMMLQ, or symmetric QMR must be used in place of Conjugate Gradients.

3.2.2.3 Skeletal Attachments

Since the surfaces of attachment between flesh and bone do not coincide with nodes of the simulation lattice, we enforce such attachments via soft, spring-based constraints. The attachment energy E_{att} is formulated as:

$$E_{\text{att}}(\mathbf{x}) = \sum_i \frac{k_i}{2} \|\mathbf{W}_i \mathbf{x} - \mathbf{t}_i\|_2^2, \quad (3.7)$$

where $\mathbf{t}_i$ is the target location (on the moving skeleton) of a flesh attachment, $\mathbf{W}_i$ is a trilinear interpolation operator that computes the interpolated location of an interior flesh point from the vector of nodal positions $\mathbf{x}$, and k_i is the stiffness parameter of the i-th attachment. Attachment points are discretely sampled as a preprocess on the bone surfaces. Attachment points are sampled uniformly, with

a target density that yields an average of 3 to 6 attachment points per cell of the simulation lattice. The stiffness parameters are adapted such that a constant stiffness per bone surface area is achieved.

3.2.2.4 Discretization Given Musculature and Skeletal Structure

We use standard trilinear hexahedral elements on a cubic lattice for the discretization of the deformation map ϕ, while the pressure field is only approximated as cell-wise constant. The geometries of the skin, muscles and bones are embedded in the simulated hexahedra. We use the geometry of the muscles to modulate the material properties assigned to each simulation element. We compute the nonlinear energy integrals by defining a 4-point quadrature rule on an individual lattice cell basis, which is designed to be accurate in the integration of polynomials of degree up to 2, yielding a (locally) second-order accurate approximation to the energy.

To achieve second-order accuracy on arbitrarily integration domains, we use a numerical quadrature scheme that integrates exactly all monomials $X^p Y^q Z^r$ with $0 \leq p + q + r \leq 2$; i.e., we provide the following quadrature (Patterson et al., 2012):

$$\int_{\Omega_k} \begin{bmatrix} 1 & X & Y & Z \\ X & X^2 & XY & XZ \\ Y & XY & Y^2 & YZ \\ Z & XZ & YZ & Z^2 \end{bmatrix} d\mathbf{X}. \tag{3.8}$$

Here $\mathbf{X} = (X, Y, Z)$ is the material point in the undeformed configuration and $\Omega_k = \Omega \cap C_k$ is the elastic sub-domain within each lattice cell C_k.

In our implementation, we use Monte-Carlo integration to compute the relevant moments of fractional cells C_k. A number of randomly generated points are uniformly distributed in each simulation hexahedron, indicated as colored

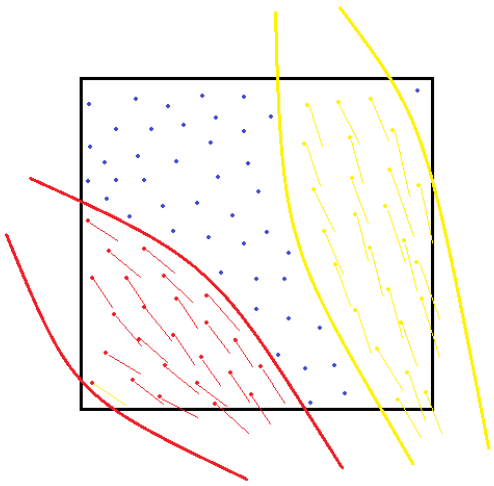

Figure 3.3: Embedding the muscles into the volumetric mesh.

dots in Figure 3.3. We use 1.6×10^6 points for each simulated hexahedron of size 20mm $\times$ 20mm $\times$ 20mm. We check whether each of these sample points is located inside any muscle volume, in which case the direction of the muscle fiber at the given location is associated with the sample point. These sample points are depicted as red and yellow vector fields in Figure 3.3, corresponding to two distinct muscles intersecting a simulation hexahedron. Points not inside any muscle volume are considered as locations of passive flesh or fatty tissue, displayed as blue dots in Figure 3.3. Using these sample points, we compute the quadrature (3.8) for the fraction of the simulation hexahedron covered by each muscle. We also compute the quadrature for boundary cells that are partially covered by muscles or passive flesh. To obtain a representative fiber direction $\mathbf{w}_k$ in (3.5), we average the fiber directions of the sample points inside the k-th muscle and normalize the result to unit length.

3.3 Water Simulation

The surrounding water in which our biomechanical human model floats is simulated according to the Navier-Stokes equations using an Eulerian fluid solver on a MAC grid, and the water surface is tracked using the particle level-set method, which is in accordance with (Enright et al., 2002) and (Foster and Fedkiw, 2001). Our simulation framework implements the necessary dynamic force couplings between the skeleton and flesh, as well as between the deformable skin surface of the virtual human and the surrounding water, in an interleaved manner.

The fluid simulation system we use is part of PhysBAM,[1] which is an object oriented C++ library capable of solving a variety of problems in computational fluid dynamics, computational mechanics, computer graphics and computer vision. The approach to model the water surface is called the *"particle level set method"* (Enright et al., 2002), which is a hybrid surface tracking method that uses massless marker particles combined with a dynamic implicit surface. This hybrid surface model has advantages of both particle evolution and level set evolution. To elaborate, level set evolution suffers from volume loss near detailed features while particle evolution suffers from visual artifacts in the surface when the number of particles is small. Conversely, the level set is always smooth, and particles retain detail regardless of flow complexity. They tend to have complementary strength and weakness, a combined approach gives superior results under a wider variety of situations.

3.3.1 Outline of the Fluid Simulation Method

The Navier-Stokes equations for describing the motion of a liquid consist of two parts. The first enforces incompressibility by dictating that mass should always

[1] See http://physbam.stanford.edu

be conserved; i.e.,

$$\nabla \cdot \mathbf{u} = 0, \tag{3.9}$$

where $\mathbf{u}$ is the liquid velocity field, and

$$\nabla = (\partial/\partial x, \partial/\partial y, \partial/\partial z) \tag{3.10}$$

is the gradient operator. The second equation couples the velocity and pressure fields and relates them through the conservation of momentum; i.e.,

$$\mathbf{u}_t = \nu \nabla \cdot (\nabla \mathbf{u}) - (\mathbf{u} \cdot \nabla)\,\mathbf{u} - \frac{1}{\rho}\nabla p + \mathbf{g}. \tag{3.11}$$

This equation models the changes in the velocity field over time due to the effects of viscosity ν, convection, density ρ, pressure p, and gravity $\mathbf{g}$. By solving and over time, we can simulate the behavior of a volume of liquid. The basic algorithm (Foster and Fedkiw, 2001) is as follows:

1. Model the static environment as a voxel grid.
2. Model the liquid volume using a combination of particles and an implicit surface.
3. Update the velocity field by solving (3.11) using finite differences combined with a semi-Lagrangian method.
4. Apply velocity constraints due to moving objects.
5. Enforce incompressibility by solving a linear system built from (3.9).
6. Update the position of the liquid volume (particles and implicit surface) using the new velocity field.

Enright *et al.* (2002) improved this algorithm by introducing a new "thickend" front-tracking technique to accurately represent the water surface and a new

velocity extrapolation method to move the surface in a smooth, water-like manner. The focus is to maintain the liquid surface itself. Particles are placed on both sides of the surface and used to maintain an accurate representation of the surface itself regardless of what may be on one side or the other. The particles are intended to correct errors in the surface representation by the implicit function.

3.4 Flesh-Water Coupling

The traditional method for coupling fluids and solids is for the solid to prescribe velocity boundary conditions on the fluid and for the fluid to provide force boundary conditions on the solid (Benson, 1992). Accordingly, we also use the velocity of the human body model skin surface to enforce the Neumann boundary condition along the surface by making the normal component of the fluid velocity equal to the normal component of the skin's velocity. To calculate the force of the fluid on the body, we would ideally integrate over the surface of the skin the pressure computed by the fluid solver.

For incompressible flow, however, the pressure (which serves as a penalty term in the Navier-Stokes computation) is both stiff and noisy, hence more or less unreliable, as discussed in (Fedkiw, 2002). While the velocity field is a primary state variable and is limited in its temporal variation due to momentum conservation, the pressure field is a byproduct of the projection of velocities into a divergence-free field, and may exhibit notably higher temporal variance than the fluid velocities. As a consequence, instead of demanding a higher degree of accuracy in the pressure computation from our underlying fluid simulation engine, we opt for a computation of fluid-to-solid forces based on fluid velocities, which are generally more accurate and temporally coherent. We use the relative velocity of the human skin with respect to the fluid to compute the hydrodynamic force and we construct a new level-set representation of the water to compute the buoyancy

force. These forces due to the water acting on the body are computed at each triangle of the skin surface and applied to the skin as external forces.

To compute the hydrodynamic force on each triangle of the skin surface, we employ a hydrodynamic force model similar to those found in (Tu and Terzopoulos, 1994; Yang et al., 2004; Lentine et al., 2011):

$$\mathbf{f} = \min\left[0, -\rho A\left(\mathbf{n}\cdot\mathbf{v}\right)\right]\left(\mathbf{n}\cdot\mathbf{v}\right)\mathbf{n}, \tag{3.12}$$

where ρ is the density of the water, A is the area of the triangle, $\mathbf{n}$ is its normal, and $\mathbf{v}$ is its velocity relative to the water. To enforce the boundary conditions in the fluid solver, we must make the normal component of the fluid velocity equal to the normal component of the solid's velocity, so we cannot use the fluid velocity on the boundary cell to compute the relative velocity as its normal component will be approximately zero. Instead, we accumulate velocities of the fluid in neighboring cells around the boundary cell in which the skin triangle lies and employ the mean local fluid velocity to compute the relative velocity $\mathbf{v}$.

The total buoyancy force acting on the floating body equals the weight of water displaced by the body. For underwater motion with the body wholly immersed, the buoyancy approximately cancels out the gravity force, since the average density of the human body approximately equals the density of water. However, this is not the case for swimming where the human body is often only partially immersed. It is then very important to compute buoyancy correctly in order to simulate realistic dynamic trunk motions, especially for the butterfly swimming stroke. We can represent the buoyancy as $\mathbf{B} = -\rho\mathbf{g}V$, where $\mathbf{g}$ is the gravitational acceleration, and V is the volume of water displaced by the body. We may rewrite this as

$$\mathbf{B} = \rho\mathbf{g}\int_S h(\mathbf{n}\cdot\hat{\mathbf{j}})dA, \tag{3.13}$$

where S is the immersed surface of the body model, $\mathbf{n}$ is the normal of the area element, $\hat{\mathbf{j}}$ is the upward unit vector, and h denotes the distance from the water

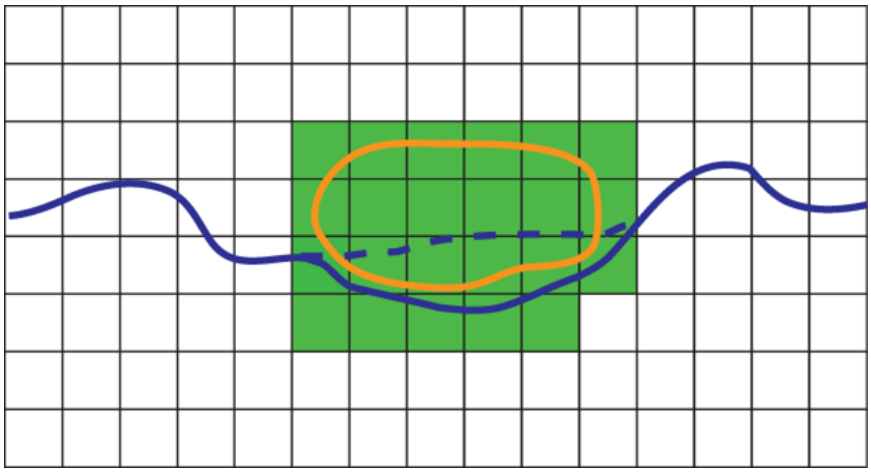

Figure 3.4: Illustration of pseudo water surface construction

surface to the area element. Thus, the force on each triangle is $\rho h A n_y \mathbf{g}$, where n_y is the y component of the normal.

The main problem is how to compute h. A simple way is using $h = y_0 - y_A$, assuming that the water surface is at a constant height y_0, where y_A is the y coordinate of the triangle center. Unfortunately, this will cause problems in the simulation, since the error can become very large when there are significant waves on the surface of the water. Even worse, the error will propagate back and forth in the interleaved two-way coupling causing an oscillation in the motion of the floating body model. We tackle this problem by constructing a *pseudo water surface (PWS)* at each time step, from which we derive h. The portion of the human body that is below this PWS is treated as the submerged part. Figure 3.4 illustrates how we construct the PWS. The yellow closed curve represents the surface of the human body and the blue solid curve represents the water surface obtained from the fluid solver. Everything below this curve is regarded as being as underwater. We determine the cells of the CFD computational grid that are inside or near the human body surface within some distance, and then we solve a minimal surface problem in this part (colored in green)—we set Dirichlet boundary conditions on the human skin surface, assigning a negative Dirichlet value for skin

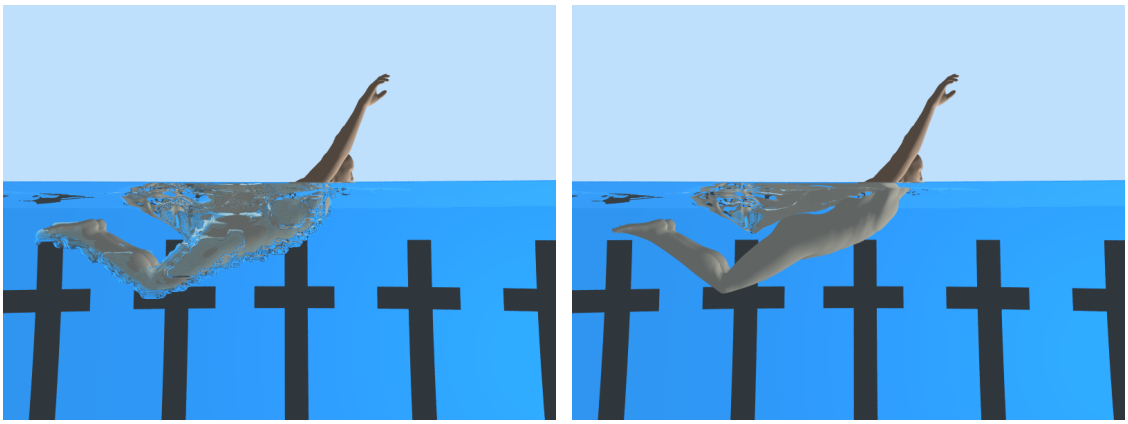

(a) Rendering with original water surface (b) Rendering with pseudo water surface

Figure 3.5: Comparison of rendering results using the original water surface (a) and the pseudo water surface (b).

regions that are immersed, and a positive value for areas of skin that are not in contact with water. We perform a harmonic interpolation between these values to reconstruct a zero isocontour of the level-set function that will extend inside the swimmer's body. Then we apply the fast marching method to obtain a level-set representation. Once this PWS has been reconstructed, we approximate the immersion depth by projecting the closest-surface-point vector ($-\phi\nabla\phi$, derived from the reconstructed level-set) along the vertical direction.

Another benefit of the PWS is that we can use it for the purposes of rendering. Figure 3.5 compares the rendering result obtained using the original water surface and that obtained using the pseudo water surface. Generally the fluid and solid surfaces are not tightly coupled because of the limit in the fluid simulation resolution, so there is a noticeable gap between the water and the human body, as is evident in Figure 3.5(a). However, since the pseudo water surface eliminates the part that is submerged, we can exploit it for rendering, so long as the solid is opaque. The much improved rendering result shown in Figure 3.5(b) is obtained using the pseudo water surface. Even when the solid is transparent, we can still use

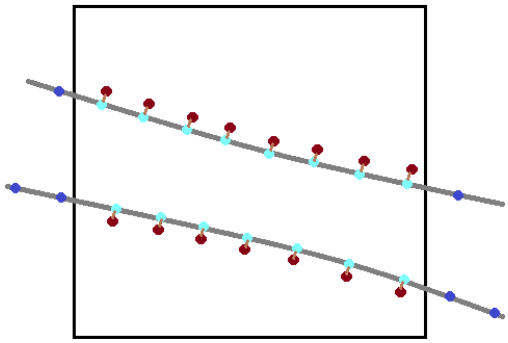

Figure 3.6: Embedding the skeleton into the volumetric mesh

the difference of the fluid volume and the solid as the new fluid volume, obtaining for example the rendering result shown in Figure 3.1.

3.5 Flesh-Bone Coupling

The deformable flesh tissue is coupled to the rigid articulated skeleton via a network of spring constraints, as has been previously demonstrated in (Lee et al., 2009) and (McAdams et al., 2011). From the viewpoint of the volumetric flesh simulation, such spring attachments serve as soft kinematic constraints. A set of particles is uniformly sampled from the surface of each bone. These particles (displayed as cyan dots in Figure 3.6 are rigidly constrained to the respective bone. We then duplicate each of these particles with the locations they have in the undeformed configuration of the body. These duplicated particles (illustrated with slight displacements as brown dots in Figure 3.6) are barycentrically embedded into the simulation hexahedron with which they overlap. Each particle attached to a bone is connected with its duplicate embedded counterpart using a zero rest-length spring. This embedded treatment of skeletal attachments decouples the

resolution of the simulation mesh from the resolution of the skeletal geometry and allows us to define the attachment regions as arbitrary point-sampled surfaces.

In our framework, we further leverage this network of soft constraints to transfer to the bones external forces that are applied to the skin surface, in a manner that respects the deformable flesh medium that separates the point of application of such forces (the skin forces) from the location of the bones. After computing the distribution of external forces on the skin, originating from any sources including fluid forces or collisions, we solve for the quasi-static equilibrium shape of the deformable flesh. Once the steady state configuration has been computed, the tension of the attachment springs is used to calculate how the skin-applied forces have been distributed to the bone-flesh interface. From balance of force properties, we have strong guarantees that the aggregate force applied by the attachment springs to the bones (at equilibrium), independent of the material parameters of the soft tissue or the stiffness of the attachment springs; of course, different material parameters may have an effect on how broadly a surface force gets spread out from the point of application. This quasi-static process makes the force translation from the flesh to the bones occur instantaneously. Although this eliminates a potential lag, the external forces on the skin or flesh are well spread to the bones in a natural way.

Appendix B discusses an for improving the flesh-bone coupling by employing the Jacobian matrix of the external translated force with respect to the generalized coordinates of the skeleton.

3.6 Summary

We have introduced a multiphysics simulation and control framework whose overall architecture is shown in Figure 1.4. The inputs to our biomechanical human model are the muscle activation levels, which drive both the Hill-type PLS muscles

that actuate the skeleton and the flesh simulation. The skeleton, flesh, and water are two-way coupled in an interleaved manner. To synthesize realistic human motion within this framework, we still need to design motor controllers that generate proper muscle activation levels to produce swimming and other aquatic motions. Our biomechanical human model also provides proprioceptive feedback, such as muscle lengths, joint angles, joint velocities, body orientation, etc., to the motor controllers. Within our simulation framework, we will proceed to develop two different types of motor controllers—locomotion controllers that produce realistic swimming and task-oriented controllers for natural underwater orientation control of the swimmer's body. Chapters 4 and Chapter 5 will present the details of these two types of controllers, respectively.

CHAPTER 4

CPG Locomotion Control

The control of biomechanically simulated human swimming is a challenging problem. Swimming motions have several distinctive styles, such as the butterfly and the crawl, each of which requires the coordinated rhythmic movement of multiple body segments.

Biological CPGs are neural networks capable of generating stable patterns of rhythmic activity without any input from higher motor control centers in the brain. In addressing biomechanical locomotion control problems such as swimming, CPG models offer important advantages, including the ability to easily modulate the rhythmic patterns. We employ CPGs to specify the desired temporally-varying length of each muscle in the swimmer's body and then apply a feedback control loop to generate the necessary muscle activation levels. This results in an easy-to-use locomotion controller that can enable various tasks, such as changing speed, turning, and transitioning between swimming strokes.

The following section details the implementation of CPG control in our biomechanical human model for the purpose of swimming simulation. Figure 4.1 shows the overall structure of our CPG locomotion control framework. The temporally-varying muscle length signals as well as their first-order and second-order derivatives serve as training data, and the necessary parameters for our CPG system are learned using Incremental Locally Weighted Regression (ILWR) (Schaal and Atkeson, 1997). The learning process, which is framed in the figure by the dashed rectangle, need only be done once, offline, and in advance. After learning, our

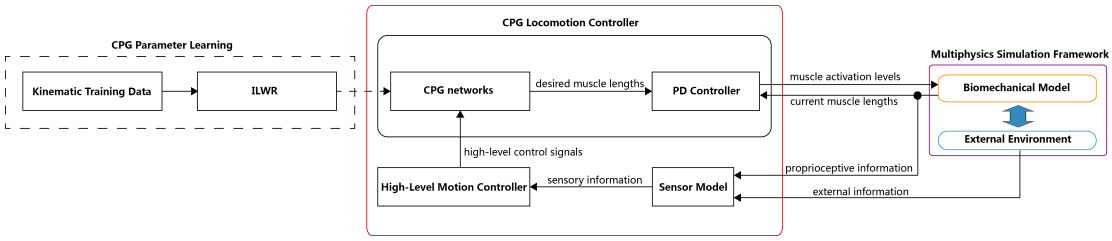

Figure 4.1: CPG locomotion control framework

CPG system can automatically generate the desired muscle length signals online, and a proportional/derivative (PD) control mechanism serves to generate the muscle activation levels. The swimmer can achieve high-level motion control by modulating the locomotion pattern via the few parameters of the CPG model.

4.1 Generating the Desired Muscle Lengths

We use (Virtual-swim, 2007) as a reference to specify key poses for our skeleton model. As CPG learning needs to use both the first and second order derivatives of the signals (see (4.5)), we want our muscle length data to be doubly differentiable. We first use cubic B-splines to fit the joint angle data in the least squares sense. After obtaining the kinematic skeleton motion, we use the distance over time between the two attachment points of each muscle as the desired time-varying length of that muscle. We fit B-splines to the desired muscle length trajectories, from whose coefficients we can easily compute the first and second order derivatives according to the B-spline differentiation formula (de Boor, 1978). Appendix C provides the computational details of these derivatives.

As is illustrated in Figure 4.2, we divide the muscles into 10 groups—left trunk, right trunk, medial trunk, left head, right head, medial head, left arm, right arm, left leg, right leg—with the muscles in each group sharing the same frequency and initial phase.[1] This division affords us flexible control over the limbs as well as

[1]Note that the muscle groups for the central trunk and the central head are less visible

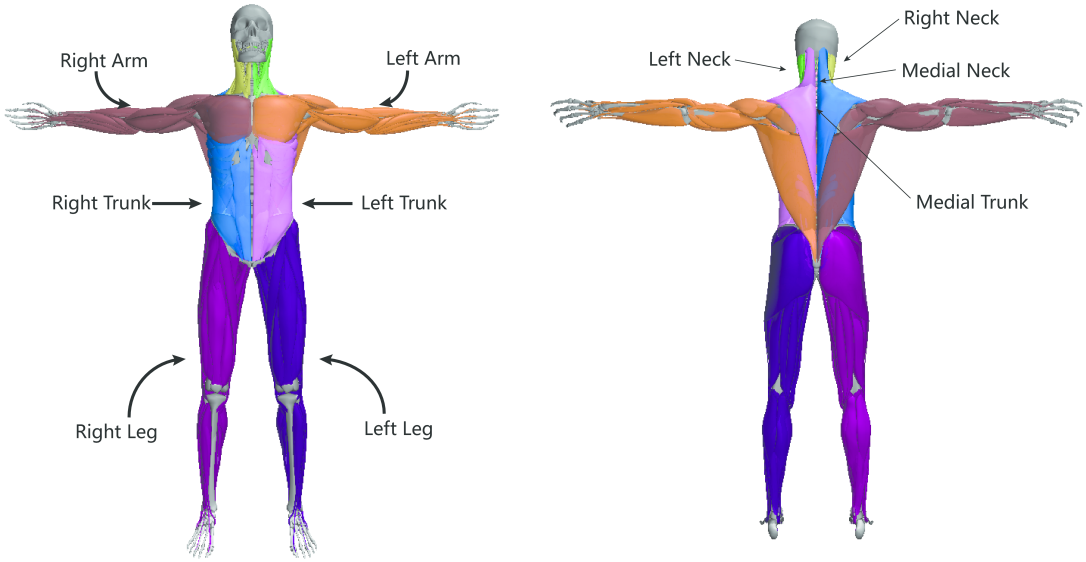

Figure 4.2: Muscle group division for CPG modeling. Each group is shown in a different color.

the trunk and head; e.g., turning is made possible by simply decreasing muscle length signals on one side and increasing muscle length signals on the other side. We will present more details about turning in Section 6.2.

4.2 CPG Learning

As is suggested in (Gams et al., 2009), we use a group of nonlinear differential equations to model each CPG unit. This model encapsulates several desirable properties, such as the reproduction of the trajectories, their modulation, and dealing with perturbations in a single set of differential equations. We explain this using a 1 DOF signal.

The following dynamics specify the attractor landscape of a trajectory y to-

because these two groups include muscles that are situated deeper in the body.

wards the anchor point g:

$$\dot{z} = \Omega \left(\alpha_z \left(\beta_z \left(g - y \right) - z \right) + \frac{\Sigma_{i=1}^{N} \Psi_i w_i r}{\Sigma_{i=1}^{N} \Psi_i} \right) \tag{4.1}$$

$$\dot{y} = \Omega z \tag{4.2}$$

$$\Psi_i = \exp\left(h \left(\cos\left(\Phi - c_i \right) - 1 \right) \right) \tag{4.3}$$

Here, $y(t)$ is the generated signal, $z(t)$ is an intermediate variable that describes the first order derivative of y, and Φ is the phase of the signal. Ω is the fundamental frequency (lowest non-zero frequency) of the input signals. Since swimming is a periodic motion, we can specify Ω as $\frac{2\pi}{T}$, where T is the period of one swimming cycle. The positive constants α_z and β_z are set to $\alpha_z = 8$ and $\beta_z = 2$ for all our simulations. The signal trajectory oscillates round g, an anchor point for the oscillatory trajectory. The number of Gaussian-like periodic kernel functions Ψ_i is N and h determines the width of the kernel function. We set $N = 25$ and $h = 2.5N$ for all our simulations, and c_i are equally spaced between 0 and 2π in N steps. The amplitude control parameter is r, which we set to 1.0.

In a single set of differential equations, the above model encapsulates several desirable properties, such as approximating the desired trajectories, offering the ability to modulate them, and maintaining robustness against perturbations.

We use ILWR to learn the weights w_i in (4.1). Locally weighted regression corresponds to finding, for each kernel function Ψ_i, the weight vector w_i that minimizes the quadratic error criterion

$$J_i = \sum_{t=1}^{P} \Psi_i(t) \left(f_{\text{targ}}(t) - w_i r(t) \right)^2, \tag{4.4}$$

where the index t denotes the discrete time step,

$$f_{\text{targ}} = \frac{1}{\Omega^2} \ddot{y}_{\text{train}} - \alpha_z \left(\beta_z \left(g - y_{\text{train}} \right) - \frac{1}{\Omega} \dot{y}_{\text{train}} \right) \tag{4.5}$$

The formulation of the above equations can be found in (Gams et al., 2009). As the input into the learning algorithm, y_{train}, $\dot{y}_{\text{train}}$ and $\ddot{y}_{\text{train}}$ are the muscle length signal, and its first and second derivatives, respectively. Incremental regression to determine the parameters w_i is accomplished with the use of recursive least squares with a forgetting factor of λ. Given the target data $f_{\text{targ}}(t)$ and $r(t)$, weight w_i is updated by

$$w_i(t+1) = w_i(t) + \Psi_i P_i(t+1) r(t) e_r(t), \tag{4.6}$$

where P is the inverse covariance matrix (Ljung and Söderström, 1983), which is updated as

$$P_i(t+1) = \frac{1}{\lambda}\left(P_i(t) - \frac{P_i(t)^2 r(t)^2}{\frac{\lambda}{\Psi_i} + P_i(t) r(t)^2}\right), \tag{4.7}$$

and

$$e_r(t) = f_{\text{targ}}(t) - w_i(t) r(t). \tag{4.8}$$

The recursion is started with $w_i = 0$ and $P_i = 1$. Batch and incremental learning regressions provide identical weights w_i for the same training sets when the forgetting factor λ is set to 1.0. Differences appear when the forgetting factor is less than 1.0, in which case the incremental regression gives more weight to recent data. In our experiments, we set $\lambda = 0.95$.

A desirable property of the CPG control model is that it allows easy modulation of the signals. Changing the parameter g modulates the baseline of the rhythmic movement. This will smoothly shift the oscillation without modifying the signal shape. Modifying Ω and r changes of the frequency and the amplitude of the oscillations, respectively. Since our differential equations are of second order, even an abrupt change of the parameters yield smooth variations of the trajectory y. Although the length trajectories of different muscles may share the same frequency, the amplitudes and baseline may vary significantly. To guarantee

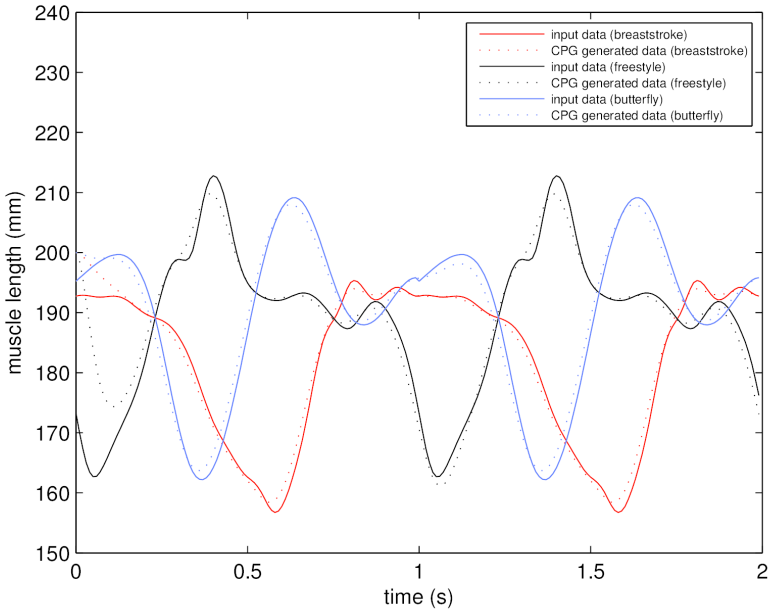

Figure 4.3: Input data and CPG generated data for the left Coracobrachialis muscle.

the quality of learning, we scale and shift each muscle length trajectory to bracket the signal between -0.5 and 0.5. For convenience, we also scale the period of the input signals to 1 second. And then use r, g, and Ω to modulate the learned signals. In the learning process, we simply set $r = 1$, $g = 0$, and $\Omega = 2\pi$.

After learning the parameters, the desired muscle length can be generated by numerically integrating (4.1), and (4.2). We employ the 4th-order Runge-Kutta method to perform the numerical integration. Φ is updated as $\Phi = \Phi + \Omega dt$, where dt is the time step. Figure 4.3 compares the input muscle length data and the CPG generated muscle length data for the left *C*oracobrachialis muscle for different swimming strokes. We can see that the CPG learns the input signal quite well. The initial output signals of the CPGs are set as 200 mm, and they rapidly match the input data.

4.3 Muscle Control

Given the CPG-generated, time-varying length for each muscle, we use a first-order PD control mechanism to compute the muscle activation level

$$a(t) = K_s(l(t) - l_d(t)) + K_d(\dot{l}(t) - \dot{l}_d(t)), \tag{4.9}$$

where $l(t)$ is the muscle length, $l_d(t)$ is the desired muscle length, and K_s and K_d are elastic and damping coefficients, respectively. In our experiments, we simply set $K_s = \frac{5}{l_0}$ and $K_d = \frac{0.005}{l_0}$, where l_0 is the natural length of the muscle, and $\dot{l}_d$ can easily be obtained as Ωz according to (4.2). As muscle activation levels range between 0 and 1, we clamp the computed $a(t)$ to the $[0, 1]$ range. The activation levels generated drive the Hill-type muscle to exert forces on the skeleton, and they also serve as inputs to the flesh simulation.

4.4 High-Level Motion Control

Our CPG-based motion controller is easy to use. After having learned several different types of swimming modes, it can easily switch and smoothly transition among these modes (by simply switching the parameters w_i, r, and g of the CPG units), perform each swimming mode at any desired frequency, phase, and amplitude (by adjusting Ω, Φ, and r, respectively), as well as achieve and maintain some desired pose (by setting $r = 0$ and not updating Φ), even for different muscle groups separately; for instance, one arm can maintain a desired pose while the remaining body parts carry out a rhythmic locomotion pattern. Regarding the transitioning between swimming modes, note that the CPG parameters can be switched abruptly since, per (4.1) and (4.2), this will cause abrupt changes only in the second derivative of the desired muscle length signal $\dot{z}$. Because Ω directly influences $\dot{y}$, so long as Ω is continuous, the desired muscle length signals will be C^1-smooth. This nice property yields natural motion transitions.

CHAPTER 5

Multiobjective Task-Oriented Control

For non-locomotive swimming motor tasks, the desired muscle contraction signals are not periodic, so we cannot use CPG-based control. Computing the desired muscle control signals from the control objective directly will be very challenging due to the large number of muscles in our biomechanical model, as well as each muscle's nonlinear behavior. Since the muscle control signals can be computed using the control approach in (Thelen et al., 2003; Lee et al., 2009) to generate the desired joint torques, we first consider our control problem in joint space and then solve it in muscle space.

However, there remain challenges to solving control problems associated with task-oriented underwater motions even in joint space. First, how should we formulate a control problem? Researchers (e.g., (Grzeszczuk and Terzopoulos, 1995; Tan et al., 2011)) have pursued spatiotemporal global optimization in order to generate natural swimming motions for simple creatures. This apparently fails to be a viable option for us. First, our human skeleton model has many more controller degrees of freedom. Second, the goal of task-oriented control might also be high-dimensional; e.g, achieving some desired body orientation or position, instead of swimming straight or following a defined path. Third, for non-locomotion tasks, vigorous limb motions can make the water environment very dynamic, thereby making it almost impossible to do sampling. Instead of attempting global optimization in time, we formulate task-oriented control as a temporally localized multiobjective optimization problem, which can be performed

much faster than global optimization, with the expectation that it will yield plausible albeit suboptimal motions when the cost function is not highly nonlinear.

To achieve the task naturally, we need to take into account three factors—task accomplishment, motion naturalness, and self collision avoidance—and the objective function of our multiobjective optimization

$$E = E_{task} + w_{nat}E_{nat} + w_{cld}E_{cld}, \tag{5.1}$$

is a weighted combination of the sub-objective function E_{task} for task accomplishment, the sub-objective function E_{nat} for making motion natural, and the sub-objective function E_{cld} for self-collision avoidance, and where w_{nat} and w_{cld} are associated weights. Self collision avoidance is easily handled as soft constraints. Our formulation must take fluid dynamics into account in order to handle the dynamics of the water environment, and we must define E_{nat} properly. To tackle the first challenge, we perform some simplifications that linearize the relationship between the external hydrodynamic forces and the joint velocities. As for motion naturalness, since there is no precise definition of natural human motion, we turn to statistical approaches, more specifically, we train a Gaussian Process Dynamical Model (GPDM) from human motion capture data and use it to define an objective function that encourages natural motion. To do task-oriented torque control, we perform this multiobjective optimization on a per-frame basis in joint space. For muscle control, we use the approach in (Lee et al., 2009) to compute muscle activation levels that generate the desired torques.

Figure 5.1 shows the overall structure of our multiobjective task-oriented control framework. To obtain the desired joint velocities, we solve an optimization problem that includes a sub-objective associated with the particular task, a motion naturalness sub-objective obtained using learned GPDMs, and a self-collision avoidance sub-objective. After that, we perform inverse dynamics to compute the necessary torques needed to generate the desired joint velocities, then we

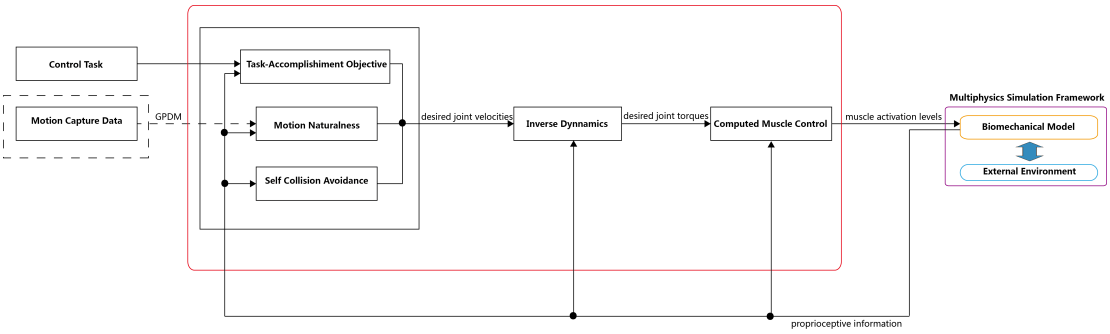

Figure 5.1: Multiobjective task-oriented control framework

solve for the muscle activation levels using the computed muscle control approach in (Lee et al., 2009). The GPDM learning (framed by the dashed rectangle in the figure) need be done just once.

To describe our formulation of task-oriented control problems in detail, let us consider controlling the orientation of the human body in water as a specific example. The task accomplishment can be formulated as achieving the desired objectives under the constraints imposed by physics. In Section 5.1 we describe the governing equation which ensures the physical validity of the motion and show the simplification process of the net hydrodynamic forces, and we formulate the objectives that are directly related to the task accomplishment in Section 5.2.

5.1 Governing Equations

The relationships between external forces and the change of net spatial momenta are as follows:

$$\mathbf{J}^{mom}\dot{\mathbf{q}} = \begin{bmatrix} \boldsymbol{\tau} \\ \mathbf{f} \end{bmatrix} \Delta t + \begin{bmatrix} \mathbf{k} \\ \mathbf{l} \end{bmatrix}, \tag{5.2}$$

where $\dot{\mathbf{q}}$ is the vector of generalized velocities, $\mathbf{J}^{mom}$ is the *centroidal momentum matrix* (Orin and Goswami, 2008) that linearly maps generalized velocities to momentum, $\boldsymbol{\tau}$ is the net external torque, $\mathbf{f}$ is the net external force, Δt is the

time step, $\mathbf{l}$ is linear momentum, $\mathbf{k}$ is the centroidal angular momentum, which is the aggregate angular momentum of the human body projected at its center of mass (CoM).

For a human body inside water, $\mathbf{f}$ comprises gravity, buoyancy, and the net hydrodynamic force. Since gravity and buoyancy approximately cancel one another, $\mathbf{f}$ is mainly the net hydrodynamic force. As seen in (3.12), for each small area of the human body, the hydrodynamic force approximately scales as the square of the relative velocity of that area with respect to the fluid. We divide the human body into m parts and assume that we can use a quadratic relationship to approximate the net hydrodynamic force for each part. In more detail, for part i, we simply use the face centers of the skin geometry triangles for that part as sampling points, and use $\mathbf{f}_i$, $\bar{\mathbf{v}}_i^s$ and $\bar{\mathbf{v}}_i^f$ to denote the net hydrodynamic force, mean velocity of the skin, and mean velocity of the fluid computed from those sampling points, respectively. We also assume that the following quadratic relationship suffices to represent the net hydrodynamic force:

$$\mathbf{f}_i = \mathbf{c}_i ||\bar{\mathbf{v}}_i^s - \bar{\mathbf{v}}_i^f||^2, \tag{5.3}$$

where $\mathbf{c}_i$ is the coefficient vector. We can compute $\mathbf{c}_i$ for each part given $\mathbf{f}_i$, $\bar{\mathbf{v}}_i^s$, and $\bar{\mathbf{v}}_i^f$. For the purposes of control, we wish to represent the net hydrodynamic force $\mathbf{f}_i$ and the corresponding net torque $\boldsymbol{\tau}_i$ as functions of the generalized velocities. We do so by finding a point $\mathbf{r}_i$ on part i that satisfies $\mathbf{v}(\mathbf{r}_i) = \bar{\mathbf{v}}_i^s$ and $\mathbf{r}_i \times \mathbf{f}_i = \boldsymbol{\tau}_i$ in the least-squares sense, where $\mathbf{v}(\mathbf{r}_i)$ is the velocity at a point $\mathbf{r}_i$. For simplicity, we use $\mathbf{v}_i^b$, interpreted as the velocity of a mean point for the i_{th} body part, to denote $\mathbf{v}(\mathbf{r}_i)$. Then we have

$$\mathbf{f}_i = \mathbf{c}_i ||\mathbf{v}_i^b - \bar{\mathbf{v}}_i^f||^2. \tag{5.4}$$

To formulate (5.2) as a quadratic programming problem, we further simplify this as a linear equation using a Taylor expansion around $\bar{\mathbf{v}}_i^s$ on the right hand side of

(5.4):

$$||\mathbf{v}_i^b - \bar{\mathbf{v}}_i^f||^2 \approx ||\bar{\mathbf{v}}_i^s - \bar{\mathbf{v}}_i^f||^2 + 2\left(\bar{\mathbf{v}}_i^s - \bar{\mathbf{v}}_i^f\right)^T \left(\mathbf{J}_i^{vel}\dot{\mathbf{q}} - \bar{\mathbf{v}}_i^f\right)$$
$$= d_i + \mathbf{e}_i^T \dot{\mathbf{q}}, \tag{5.5}$$

where $\mathbf{J}_i^{vel}$ is the Jacobian matrix that linearly maps $\dot{\mathbf{q}}$ to $\mathbf{v}_i^b$, and

$$d_i = ||\bar{\mathbf{v}}_i^s - \bar{\mathbf{v}}_i^f||^2 - 2\left(\bar{\mathbf{v}}_i^s - \bar{\mathbf{v}}_i^f\right)^T \bar{\mathbf{v}}_i^f, \tag{5.6}$$

$$\mathbf{e}_i^T = 2\mathbf{J}_i^{vel^T}\left(\bar{\mathbf{v}}_i^s - \bar{\mathbf{v}}_i^f\right). \tag{5.7}$$

Substituting (5.5) into (5.4) yields

$$\begin{bmatrix}\boldsymbol{\tau}\\ \mathbf{f}\end{bmatrix} = \begin{bmatrix}\sum \boldsymbol{\tau}_i\\ \sum \mathbf{f}_i\end{bmatrix} = \sum \begin{bmatrix}\mathbf{r}_i \times \mathbf{c}_i\\ \mathbf{c}_i\end{bmatrix}\left(d_i + \mathbf{e}_i^T\dot{\mathbf{q}}\right) \tag{5.8}$$

We substitute this into (5.2) to obtain a linear equation for $\dot{\mathbf{q}}$:

$$\mathbf{A}\dot{\mathbf{q}} = \mathbf{b}, \tag{5.9}$$

where

$$\mathbf{A} = \mathbf{J}^{mom} - \sum \begin{bmatrix}\mathbf{r}_i \times \mathbf{c}_i\\ \mathbf{c}_i\end{bmatrix}\mathbf{e}_i^T \Delta t \tag{5.10}$$

and

$$\mathbf{b} = \sum \begin{bmatrix}\mathbf{r}_i \times \mathbf{c}_i\\ \mathbf{c}_i\end{bmatrix} d_i \Delta t + \begin{bmatrix}\mathbf{k}\\ \mathbf{l}\end{bmatrix}. \tag{5.11}$$

The governing equation (5.2) should be used as a constraint in our control problem. We use a quadratic objective function to treat it as a soft constraint $E_{gov} = ||\mathbf{A}\dot{\mathbf{q}} - \mathbf{b}||^2$.

Next, we will formulate the objectives that are directly related to task accomplishment.

5.2 Task-Related Objectives

In order to make the human body rotate efficiently, we want the torque along the desired rotation axis to be as large as possible, so we use a linear objective function

$$E_{rot} = -\boldsymbol{\omega}^T \boldsymbol{\tau} \tag{5.12}$$

to achieve this, where $\boldsymbol{\omega}$ is the desired rotation axis. This E_{rot} is very important in order to generate efficient rotational motion. When the human body reaches some pose limit, it is possible that the body may rotate in the reverse direction, this linear term is very effective in mitigating this undesired effect. In general, humans tend to twist their trunk to guide the rotation of their body, so we use

$$\mathbf{J}^{trkvel}\dot{\mathbf{q}} = \mathbf{v}_{des}^{trk} \tag{5.13}$$

as a soft constraint to achieve the trunk twisting effect; i.e.,

$$E_{trk} = ||\mathbf{J}^{trkvel}\dot{\mathbf{q}} - \mathbf{v}_{des}^{trk}||^2. \tag{5.14}$$

For the orientation control problem, $\mathbf{v}_{des}^{trk}$ is the desired trunk angular velocity and $\mathbf{J}^{trkvel}$ is the Jacobian matrix that linearly maps $\dot{\mathbf{q}}$ to the trunk angular velocity. We use the orientation and velocity of the first thoracic vertebra to represent the trunk orientation and velocity. The desired angular velocity is computed using a feedback rule:

$$\mathbf{a}_{des}^{trk} = k_p \log\left(\mathbf{R}_{des}^{-1}\mathbf{R}\right) - k_d \mathbf{v}^{trk} \tag{5.15}$$

$$\mathbf{v}_{des}^{trk} = \mathbf{v}_{trk} + \mathbf{a}_{des}^{trk}\Delta t, \tag{5.16}$$

where $\mathbf{R}_{des}, \mathbf{R} \in \mathrm{SO}(3)$ are the desired trunk orientation and the current trunk orientation respectively, k_p and k_d are proportional and derivative feedback gains, respectively, and $\mathbf{v}^{trk}$ is the current angular velocity of the trunk.

In summary, the orientation control objective function for task accomplishment can be formulated as a weighted combination of the sub-objective functions; i.e.,

$$\begin{aligned} E_{orient} &= E_{gov} + w_{trk}E_{trk} + w_{rot}E_{rot} \\ &= ||\mathbf{A}\dot{\mathbf{q}} - \mathbf{b}||^2 + w_{trk}||\mathbf{J}^{trkvel}\dot{\mathbf{q}} - \mathbf{v}_{des}^{trk}||^2 \\ &\quad - w_{rot}\boldsymbol{\omega}^T \sum \mathbf{r}_i \times \mathbf{c}_i \left(d_i + \mathbf{e}_i^T \dot{\mathbf{q}}\right) \end{aligned} \tag{5.17}$$

This is a quadratic function of $\dot{\mathbf{q}}$. Note that $\mathbf{r}_i$, $\mathbf{c}_i$, d_i, and $\mathbf{e}_i$ are updated per frame. We set $w_{trk} = 1$ and $w_{rot} = 1000$ for all the results presented in this thesis.

5.3 Naturalness

Although we can achieve orientation control by minimizing E_{orient}, the resulting motion might be very unnatural (see Chapter 6). The motion unnaturalness may originate from multiple sources, but there are two common cases among them. First, the human body may run into some unnatural pose, even though the joint limits are satisfied. Second, the motion may not be fluid even though the pose itself is natural; e.g., the human body is stuck in some pose for a while. We could easily run into these cases if we simply optimize E_{orient} alone without a term that encourages natural poses in E_{orient} and it is also very likely to get stuck in some solution temporarily because of the temporal locality of our optimization scheme. In order to handle these cases, we use the GPDM, which encodes both pose naturalness and temporal dynamics information of the motion, to provide a preferred solution $\dot{\mathbf{q}}_{nat}$ and define an objective function

$$E_{nat} = ||\dot{\mathbf{q}} - \dot{\mathbf{q}}_{nat}||^2. \tag{5.18}$$

To obtain $\dot{\mathbf{q}}_{nat}$, we first solve for a latent point $\mathbf{x}_{nat}$ that defines the natural pose (or velocity) by minimizing

$$\begin{aligned} E_{nat}\left(\mathbf{x}_{t+1}\right) &= E^{\mathbf{x}}_{orient} + w_{prior}E_{prior} \\ &\quad + w_{smooth}E_{smooth} + w_{confid}E_{confid} \\ &= E_{orient}\left(\dot{\mathbf{q}}\left(\mu_Y(\mathbf{x}_{t+1})\right)\right) - w_{prior}\ln p\left(\mathbf{X}^{(*)}|\Gamma\right) \\ &\quad + w_{smooth}||\mu_Y(\mathbf{x}_{t+1}) - \mu_Y(\mathbf{x}_t)||^2 \\ &\quad + w_{confid}\sigma^2_Y(\mathbf{x}_{t+1}). \end{aligned} \tag{5.19}$$

This objective function is defined similarly to (Levine et al., 2012), which uses the GP to map the joint space to latent space and defines the motion quality term using a latent space motion prior, smoothness, as well as the prediction variance of the reconstruction GP. In detail, $\mu_Y(\mathbf{x})$ is the mean of the GP for pose reconstruction as a function of the latent space position $\mathbf{x}$, Γ is the learned GPDM model parameters. $\mathbf{X}^{(*)}$ is the latent trajectory. In our application, we use three adjacent latent points as $\mathbf{X}^{(*)}$; i.e., $\mathbf{X}^{(*)} = [\mathbf{x}_{t-1}, \mathbf{x}_t, \mathbf{x}_{t+1}]^T$. $\sigma^2_Y(\mathbf{x})$ is the prediction variance. In this equation, $E^{\mathbf{x}}_{orient} = E_{orient}\left(\dot{\mathbf{q}}\left(\mu_Y(\mathbf{x}_{t+1})\right)\right)$ prefers solutions that are consistent with the orientation control objective, and $E_{prior} = -\ln p\left(\mathbf{X}^{(*)}|\Gamma\right)$ encourages output motion to be close to the training data. Another big advantage of this E_{prior} is that it makes the motion fluid, preventing the human body from becoming stuck in some pose due to local optimality or a joint limit. $E_{smooth} = ||\mu_Y(\mathbf{x}_{t+1}) - \mu_Y(\mathbf{x}_t)||^2$ measures the smoothness of the motion in feature space, $E_{confid} = \sigma^2_Y(\mathbf{x}_{t+1})$ measures the confidence of the reconstructed pose from the latent position and prefers natural poses that are closer to the training data. Although E_{prior} partially overlaps with E_{smooth} and E_{confid} in terms of functionality, we found that having E_{smooth} and E_{confid} explicitly in the objective function results in easier and more intuitive control of different sub-objectives. The exact definition of $\mu_Y(\mathbf{x})$, $p\left(\mathbf{X}^{(*)}|\Gamma\right)$, and $\sigma^2_Y(\mathbf{x})$ can be found in (Wang et al., 2008). Due to a nice property of the GP, we can efficiently compute $\partial E_{nat}/\partial \mathbf{x}_{t+1}$

analytically. With this partial derivative, we can efficiently solve a nonlinear optimization problem; i.e.,

$$\mathbf{x}_{nat} = \arg\min_{\mathbf{x}_{t+1}} E_{nat}\left(\mathbf{x}_{t+1}\right) \tag{5.20}$$

to obtain a latent point $\mathbf{x}_{nat}$ that defines the natural pose (or velocity). Experiments show that we can generally find a decent suboptimal solution. Then we can compute $\dot{\mathbf{q}}_{nat}$ from $\mu_Y(\mathbf{x}_{nat})$. In our application, we use joint angles (pose) as the feature vector $\mathbf{y}$ for the GPDM and compute $\dot{\mathbf{q}}\left(\mu_Y(\mathbf{x}_{t+1})\right)$ in (5.19) as well as $\dot{\mathbf{q}}_{nat}$ using the numerical pose difference. We can initialize $\mathbf{x}_0$ by minimizing $||\mathbf{q}_0 - \mu_Y(\mathbf{x})||$.

After we impose E_{nat}, it is possible that this sub-objective will conflict with E_{orient}, which may result in reverse rotation; however, the existence of the linear term E_{rot} will largely mitigate this effect. In practice, we always achieve the desired orientation after several trials.

In our application, to make the latent space more powerful and flexible in representing motion space from limited training data, we train four GPDM models for the respective limbs independently with a connectivity prior as suggested in (Levine et al., 2012). We fill in $E^{\mathbf{x}}_{orient}$ with latent points that are defined within these GPDM models and leave unmodified the joints (e.g., joints that correspond to the trunk bones) that are not specified by any latent space. We define the other sub-objectives to be the summation of the limb GPDM sub-objectives; i.e., $E_{prior} = \sum_{j=1}^{4} E^j_{prior}$, $E_{smooth} = \sum_{j=1}^{4} E^j_{smooth}$ and $E_{confid} = \sum_{j=1}^{4} E^j_{confid}$. Note that even with all of these, minimizing E_{nat} by itself does not result in motion that achieves the desired orientation, although we have the orientation sub-objective term in (5.19). In fact, the solved motion is quite inefficient in orientation control due to the limited training data and the inadequate capacity of the GPDM to handle large, heterogeneous datasets. However, it serves very well to make the resulting motion natural. For the experimental results we present in this thesis,

we set $w_{prior} = 5 \cdot 10^{-7}$, $w_{smooth} = 0.5$, and $w_{confid} = 5$.

5.4 Collision Constraints

Self-collision avoidance is handled via soft constraints as in (Ho et al., 2010). Collision constraints can be applied through the following equation:

$$\mathbf{C}\dot{\mathbf{q}} = \mathbf{v}^c_{des}. \tag{5.21}$$

Row i of this equation is

$$\mathbf{n}_i^T \left(\mathbf{J}_i^{C1} - \mathbf{J}_i^{C2}\right) \dot{\mathbf{q}} = v_i^{des}, \tag{5.22}$$

where $\mathbf{n}_i$ is the unit vector computed from the i_{th} closest point pair on the colliding bodies, $\mathbf{J}_i^{C1}$ and $\mathbf{J}_i^{C2}$ are the Jacobian matrices that map the generalized velocities to the velocities of the closest point pair, and v_i^{des} is the desired relative velocity of the point pair in the $\mathbf{n}_i$ direction. We use the exponential of the penetration depth to compute v_i^{des}. To detect self-collision, we bound each body segment by a capsule. We also treat the collision constraints as soft constraints; i.e.,

$$E_{cld} = ||\mathbf{C}\dot{\mathbf{q}} - \mathbf{v}^c_{des}||^2. \tag{5.23}$$

5.5 Solution

We substitute (5.17), (5.19), and (5.23) into (5.1) with $E_{task} = E_{orient}$, and solve the quadratic programming problem

$$\dot{\mathbf{q}}_{des} = \arg\min_{\dot{\mathbf{q}}} E\left(\dot{\mathbf{q}}\right). \tag{5.24}$$

After solving for $\dot{\mathbf{q}}_{des}$, we perform inverse dynamics to compute the necessary torques to achieve $\dot{\mathbf{q}}_{des}$, and then solve for muscle activation levels using the muscle control approach in (Lee et al., 2009). For all our experimental results, we set

$w_{nat} = 1$ and $w_{cld} = 10^{-4}$. We use the time step of the training data sampling to update the latent space optimization solution in (5.20) while using a smaller time step to update the joint space optimization solution in (5.24).

All the Jacobian matrices can be computed efficiently in an analytical way within our multibody system framework. Although our formulation is local in time, it generates decent motion that achieves the desired orientation naturally. All of the optimization problems are solved using sequential quadratic programming (Gill et al., 2002). The partial derivatives needed for optimization are given in Appendix D. When doing optimizations in joint space, the joint limits are used to set the boundary constraints in order to ensure that the joint limits are respected.

Note that if we use linear velocity in defining (5.13) and modify the linear term in (5.12) to be a force projected in the desired direction, the controller can serve as a translation controller to achieve the desired position. This formulation and the idea of employing a GPDM for physics-based control can also be generalized to a wider range of task-oriented control problems.

CHAPTER 6

Experiments and Results

In this chapter, we present experimental results obtained within our simulation and control framework, including synthesizing various swimming strokes and body-orienting maneuvers in water.[1]

On a 2.8GHz Intel i7 CPU with 4GB of RAM, the running times of our swimming simulator with a 192 fps frame rate range from 3 to 10 minutes per frame, depending on how many steps the adaptive time-stepping fluid and deformable solid simulators execute per frame. The overhead for stepping the controller is negligible compared to the cost of the physics-based simulation.

For all the experiments presented, the water density is set to 1000 kg/m^3 and the Young's modulus of the human flesh to 5×10^5 N/m^2, following (Agache et al., 1980). The average density of our human model is 980 kg/m^3.

6.1 Swimming Strokes

We trained our CPG control system on two different swimming strokes—crawl and butterfly—illustrated in Figures 6.1 and 6.2.

[1] Our results are demonstrated in an an accompanying video.

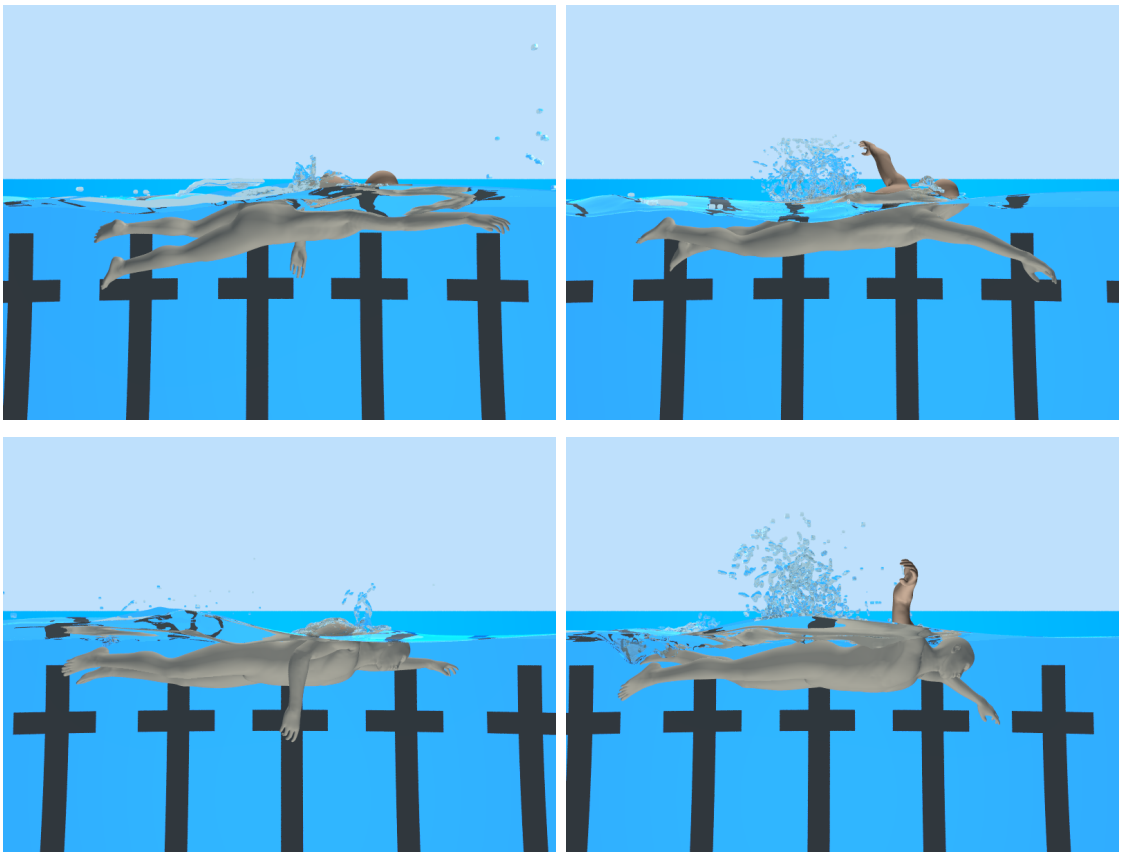

Figure 6.1: Crawl swimming sequence

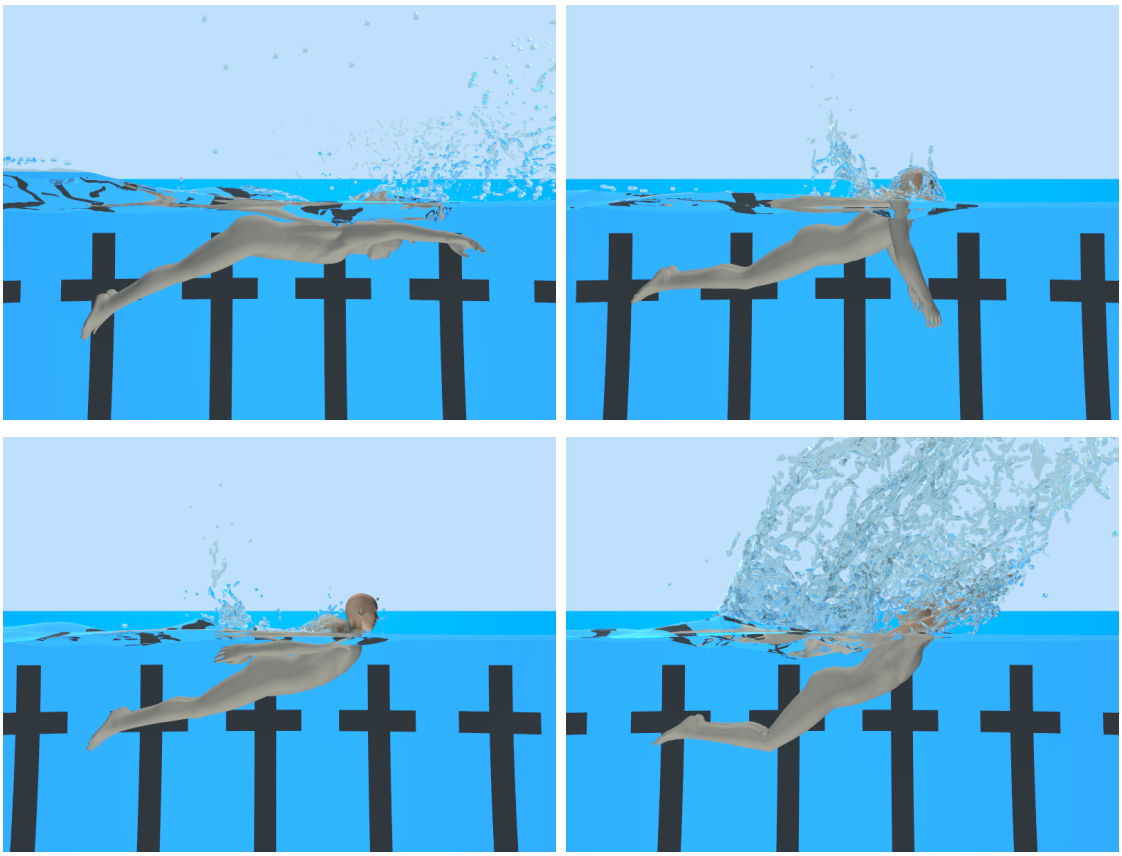

Figure 6.2: Butterfly swimming sequence

6.2 Swimming Motion Modulation

In addition to generating coordinated swimming motion, our CPG controller can also achieve more complex tasks by modulating a few high-level parameters. The swimming speed can be modulated by scaling the fundamental frequency Ω of each muscle group by the same amount. In order to generate a natural transition, we can change the frequency gradually to the desired frequency. Figure 6.3 shows an animation sequence (frames separated by 1 sec) of a simulation in which we increase the speed of the butterfly stroke by doubling the fundamental frequency.

Swimming stroke transitions are accomplished by switching the parameters (w_i, r, and g) of the CPG units from one motion to a different motion. Figure 6.4 illustrates an animation sequence that demonstrates the transition from butterfly to crawl swimming.

To produce a left turn, the g of left neck and left trunk muscles are decreased, the g of the right neck and right trunk muscles are increased, and the r for all the neck and trunk muscles is decreased. Right turns are produced by doing the opposite. Figure 6.5 illustrates an animation sequence of the swimmer following a moving target, the white ball, with turning functionality in the butterfly swimming stroke. To execute sharp turns, our virtual swimmer can keep one arm straight by switching the CPG parameters of that arm muscle group to a static pose ($r = 0$). Figure 6.6 shows an animation sequence of the virtual swimmer making a 90-degree right turn.[2] Figure 6.7 shows the trajectory of the body from the top view.

[2]This is similar to the turn demonstrated by a (real) swimmer just after 1:22 in the YouTube video at the following url: https://www.youtube.com/watch?v=YLT7YEwUCwI.

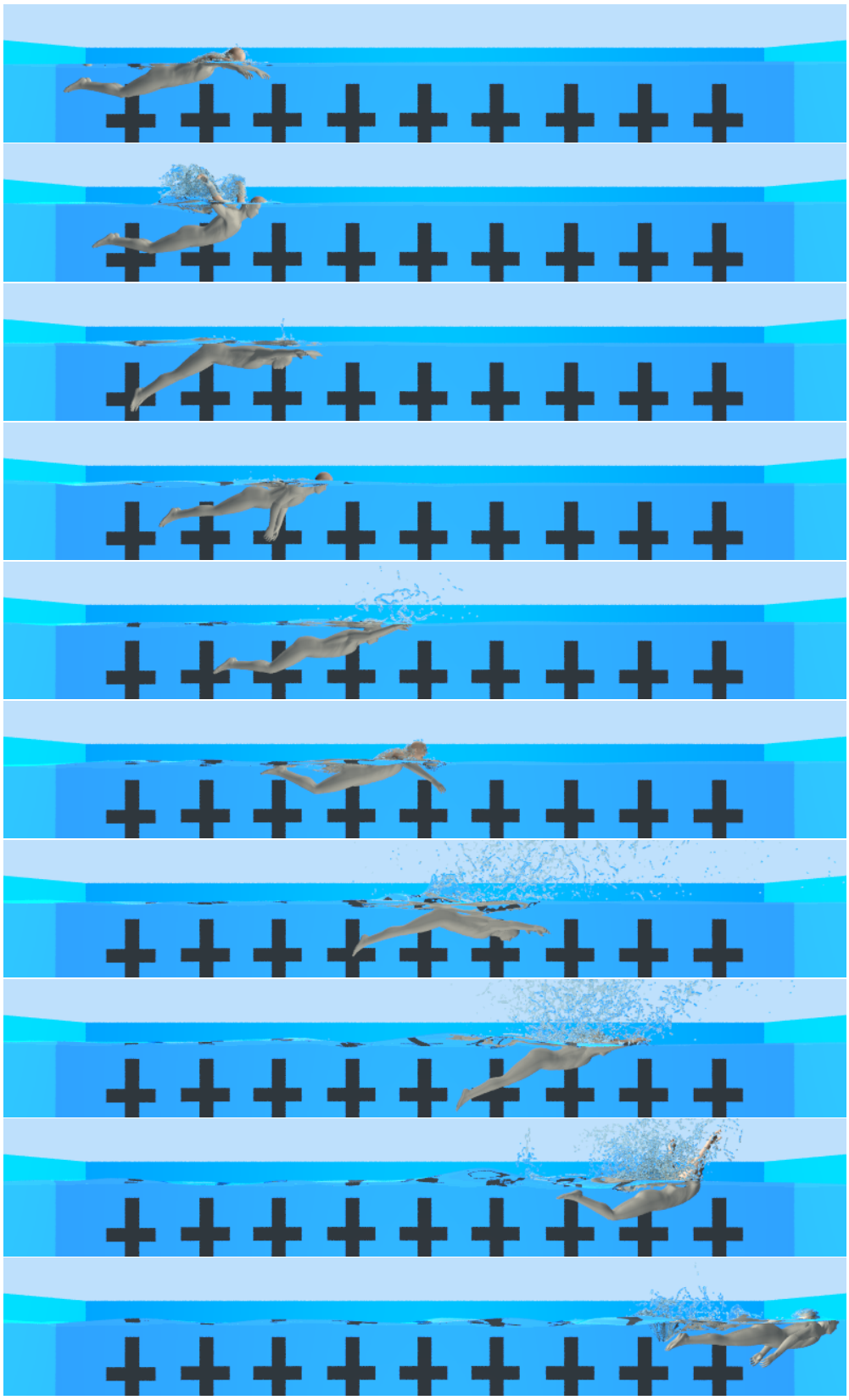

Figure 6.3: Increasing the swimming speed

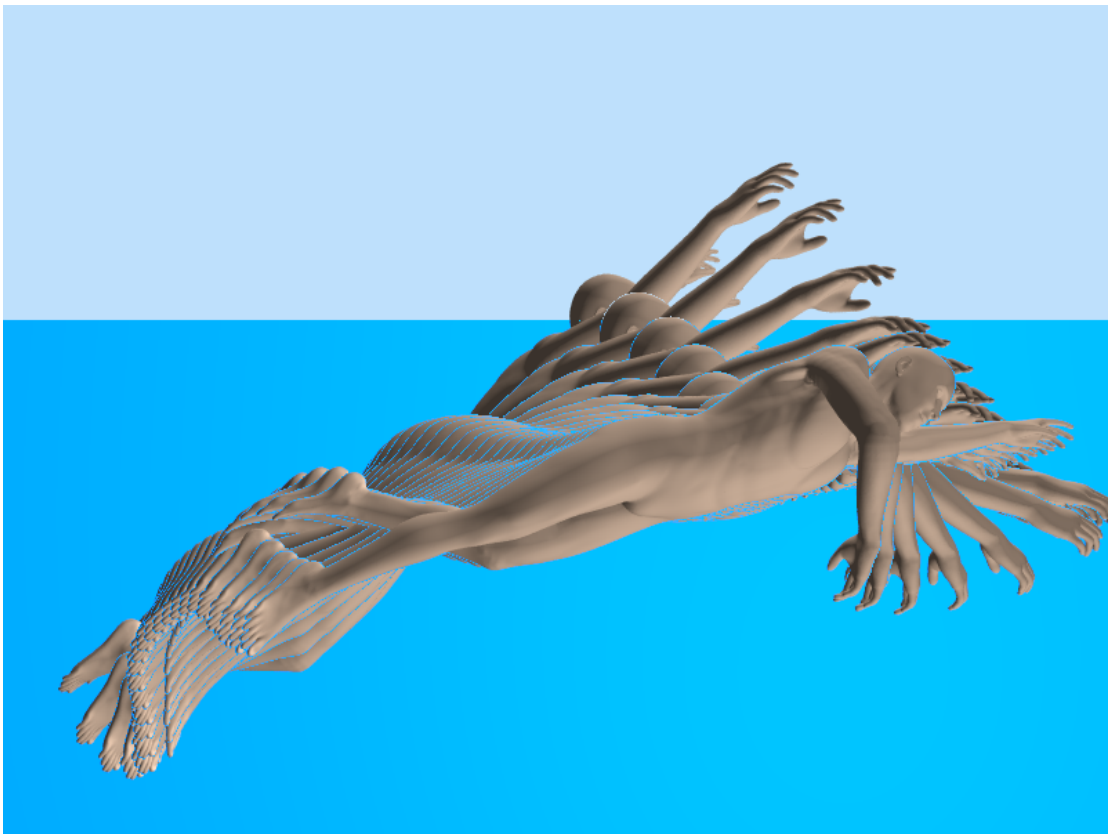

Figure 6.4: Transition from butterfly to crawl

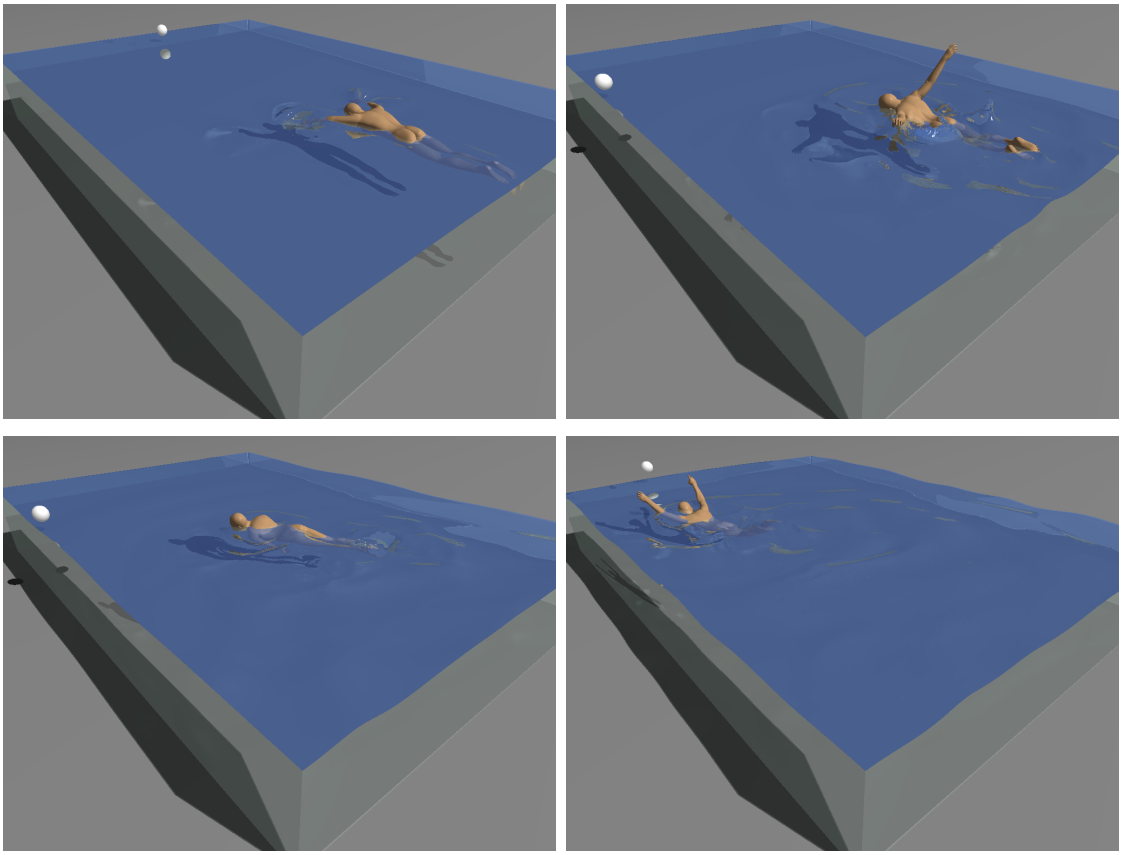

Figure 6.5: Turning to follow a moving target white ball using the butterfly swimming stroke

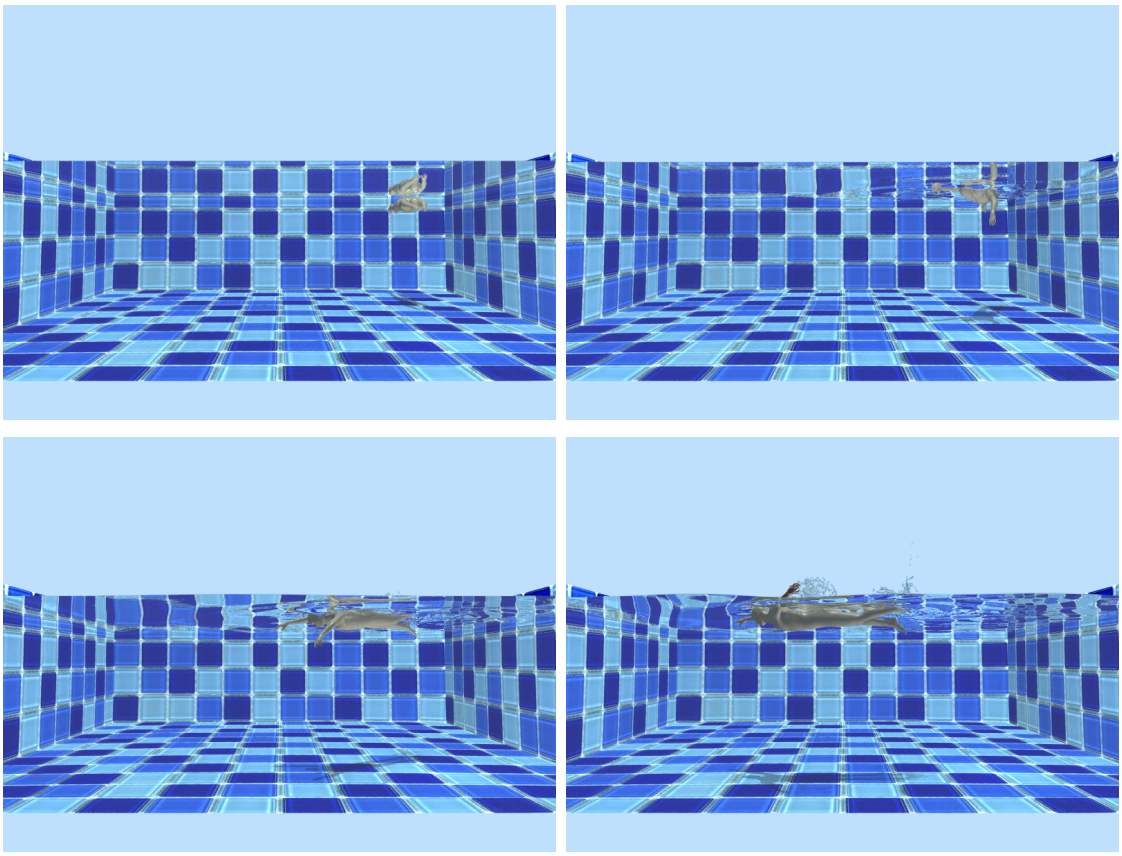

Figure 6.6: Executing a 90-degree right turn using the crawl swimming stroke

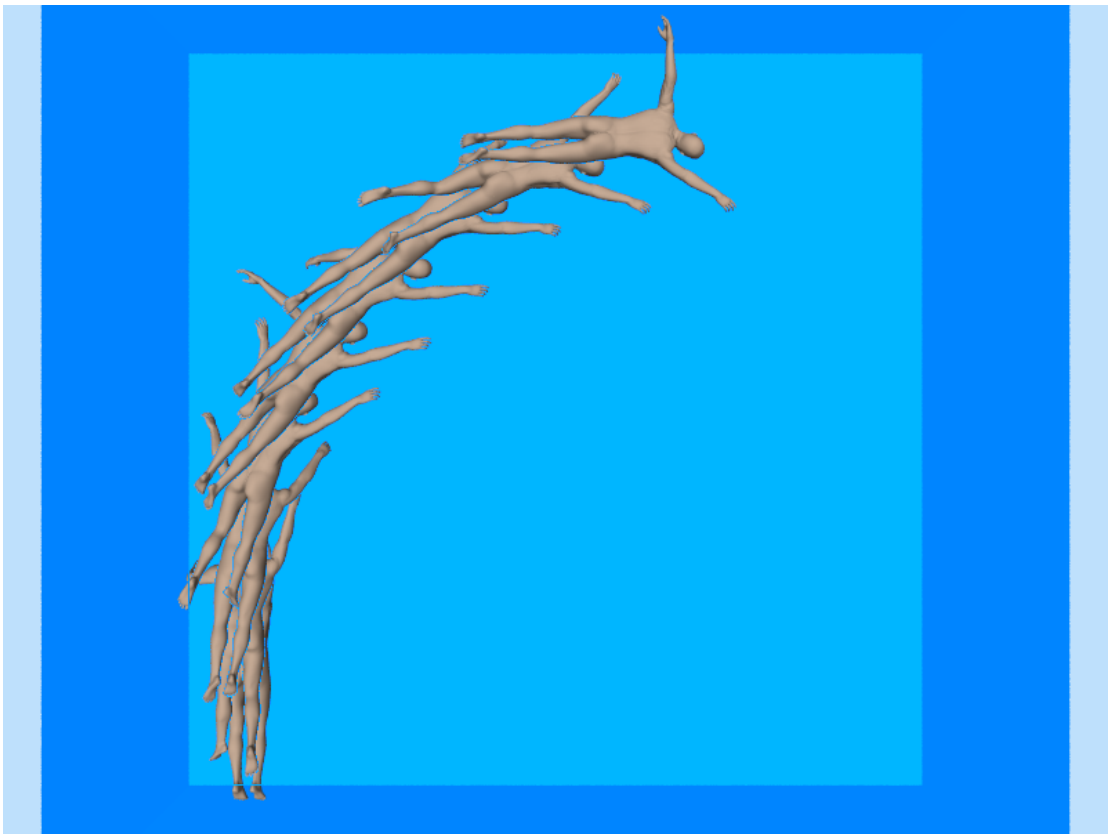

Figure 6.7: Turning sequence

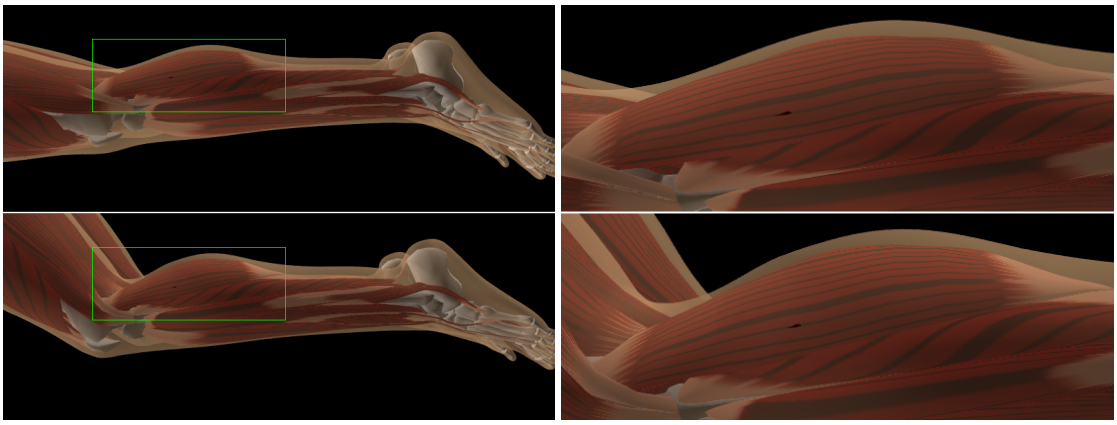

Figure 6.8: Contraction and bulging of the Gastrocnemius muscle (from the butterfly swimming simulation)

6.3 Anatomically Detailed Simulation

With all the elements involved in our multiphysics simulation framework for human swimming, we can also demonstrate the detailed anatomical animation of the human body by rendering the skin translucently. Figure 6.8 shows two close-up views (frames separated by 0.594 sec in time) from a simulation, in order to illustrate the contraction and bulging of the *Gastrocnemius* muscle.

6.4 Orientation Control

We have applied the orientation controller that we developed in Chapter 5 to achieve two tasks—turn to a supine orientation (Figure 6.9) and a prone orientation (Figure 6.10). To demonstrate the importance of the GPDM-based naturalness objective function, we turn off this objective in the task of turning to a supine orientation by setting $w_{nat} = 0$ in (5.1). Our simulation shows that the right arm is stuck for quite some time in the task accomplishment process and the motion is much less natural compared to the result with the naturalness objective turned on. Figure 6.11 compares the animation sequences of these two

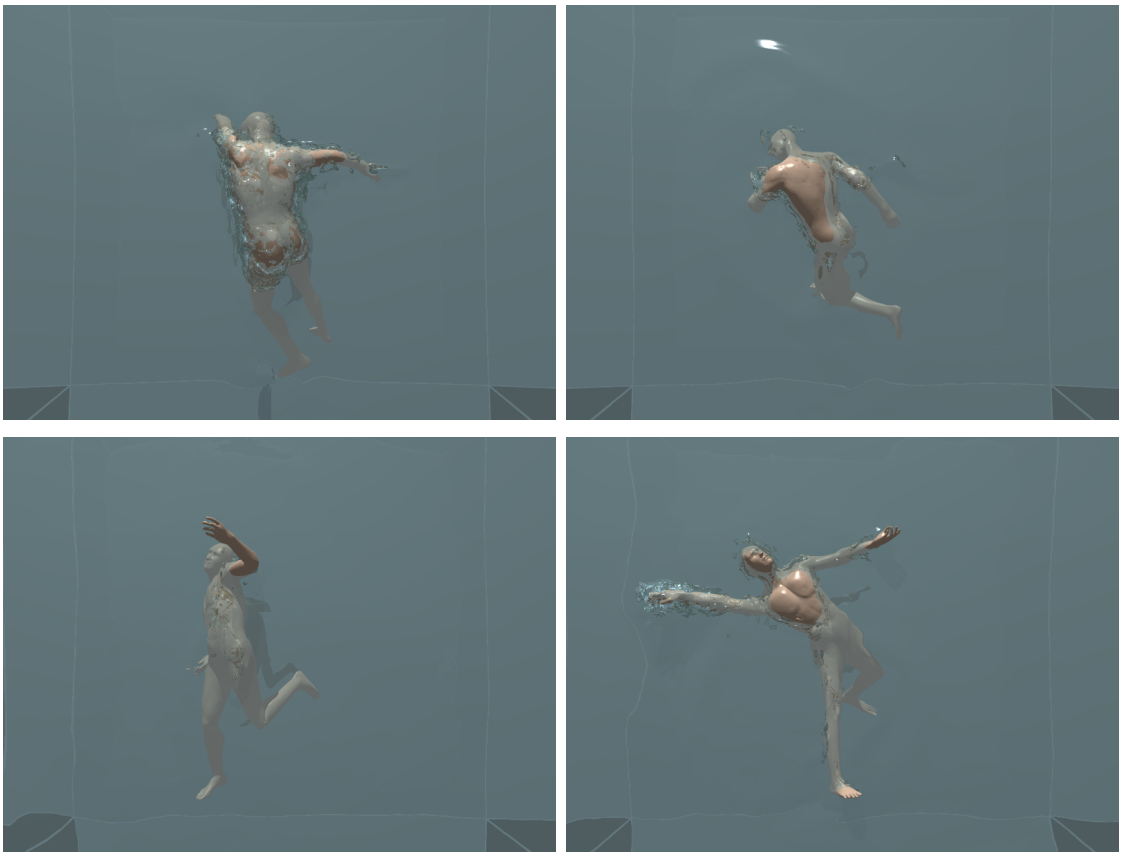

Figure 6.9: Frames from a simulation sequence for the task of turning to a supine orientation

simulations.

Figure 6.10: Frames from a simulation sequence for the task of turning to a prone orientation

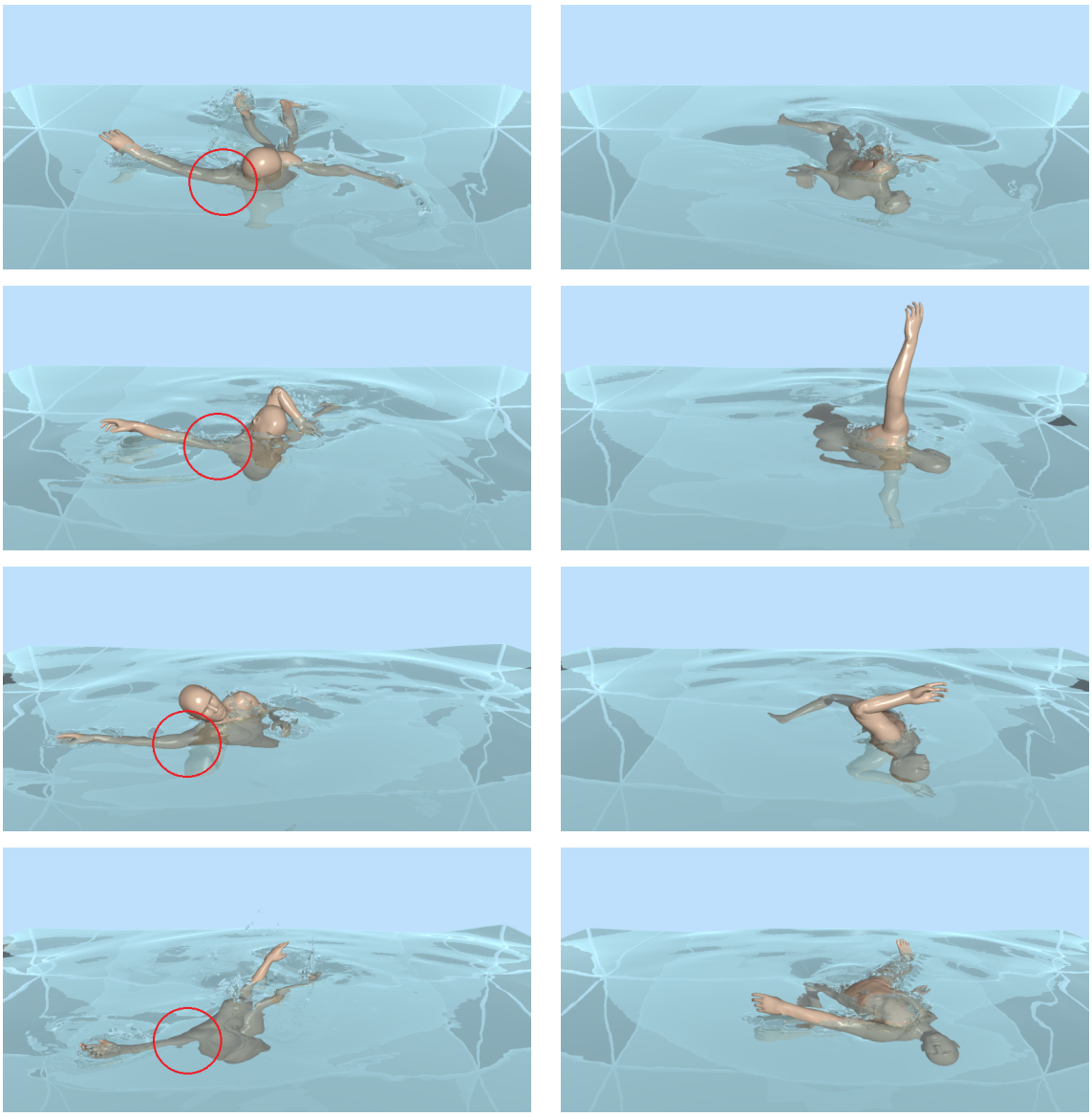

Figure 6.11: (left) GPDM-based naturalness objective off (note that the right arm remains stuck). (right) GPDM-based naturalness objective on.

CHAPTER 7

Discussion

Our interleaved approach to coupling fluid, flesh, and skeletal components provides us flexibility and versatility in constructing our simulation and control framework from different algorithmic building blocks and simulation algorithms. However, interleaved coupling reflects a conscious compromise in traits such as stability, accuracy, and performance potential. A more tightly-coupled system with deformable, fluid, and rigid components would, in theory, enable implicit time-integration techniques that would achieve stable simulation while tolerating larger time steps. In contrast, we take the most time-step-restrictive of the phases involved (generally the fluid) and use it to dictate the time-step for the entire interleaved simulation cycle. As controllers and modular simulation components mature, a tightly-coupled multiphysics-control system would certainly be appropriate.

Although the interleaved coupling of skeleton, flesh, and fluid provide flexibility and ease in constructing the simulation framework, they also compromise stability, accuracy, and performance. We sacrifice accuracy for stability in our fluid-skin coupling by using the reliable velocity field rather than the unreliable pressure field to compute hydrodynamic forces on the body. To employ pressure, we would need a better fluid solver and/or a better coupling method. For the flesh-skeleton coupling, we sacrifice performance for stability and accuracy. In order to produce stable flesh-skeleton simulation under large environmental perturbation (e.g., ground collision), we would have to take very small time steps. This could

be aided by computing a Jacobian matrix, which represents the flesh force change acting on the bones with respect to the skeleton pose change, and use it in an implicit integration of the multibody dynamics system.

Our combined use of PLS muscle forces and forces stemming from the volumetric flesh simulation has an interesting consequence. The mechanical response of the skeleton to a specific pose includes force components arising from both the PLS model and the volumetric simulation. For example, reactive forces act on the bones as the body pose causes stretching or compression of the flesh. Such a response serves a similar purpose as the passive component of PLS muscles. In addition, since our flesh simulation incorporates active musculature, the contraction of such volumetric muscles will transmit forces to their attached bones. In an ideal setting, the volumetric simulation would capture the entirety of forces due to flesh elasticity and muscle contraction alike. However, obtaining accurate muscle forces exclusively from the volumetric simulation requires a great degree of modeling accuracy, including detailed geometric and material descriptions for tendons and connective tissues. This is a significantly higher standard of modeling detail and accuracy than would be necessary for recreating natural looking flesh deformations, where the accuracy of deep muscle forces is not a crucial factor. On the other hand, while the PLS approximation does not provide information on volumetric deformation, it is capable of reproducing stable and biomechanically faithful muscle forces and torques. Our approach has been to include both sources of force, and use each to compensate for inaccuracies in the other. For example, in the absence of tendon models in the volumetric flesh simulation, the effect of muscle contraction on bones is greatly diluted, and spread out over a broader area than the actual point of attachment; this is compensated by relying on the PLS model to contribute the bulk of the articulatory forces. On the other hand, the transfer of forces acting on the skin to the bones via the elastic flesh relies almost exclusively on the volumetric simulation. Ultimately, we

treat the combined PLS/volumetric simulation system as a combined anatomical approximation whose parameters are adapted to produce realistic simulation.

We will next report on an additional set of experiments aimed at assessing the importance of various simulation/control components of our framework relative to alternative approaches.

7.1 CPG Control vs. Splines

On a fundamental level, we advocate CPG-based locomotion control, since the CPG is a principled low-level motor control mechanism from a biological perspective. However, spline-based animation methods have traditionally been more familiar to graphics practitioners. In fact, as discussed in Section 4.1, we initially use cubic B-splines to approximate the CPG training data. As a simple alternative to the CPG dynamical model, our continuous spline approximations may be repeated in time to produce periodic muscle signals to drive our virtual swimmer. The accompanying video includes a comparison of our CPG-controlled swimming against spline-controlled swimming. Although the results look qualitatively similar for any particular swimming stroke in steady state, the spline technique is noticeably choppier than the CPG technique due to discontinuities in the derivatives of the periodic spline functions across cycles, whereas the muscle control signals generated by our CPGs are always C^1 smooth. Moreover, to switch from one swimming stroke to another, the spline-based controller would have to transition carefully between numerous periodic spline functions, one per muscle. By contrast, our CPG muscle controllers can effect smooth transitions and control swimming speed by simply switching and/or modifying the values of a few parameters.

7.2 Muscle Control vs. Joint Torques

On a fundamental level, we advocate muscle-based control as contractile muscles are the principled skeletal actuation mechanism from a biological perspective. However, joint-torque animation control methods have traditionally been more familiar to graphics practitioners. Since skeletal muscle forces, through (bone) moment arms, eventually produce torques at rotational joints in the skeleton (but see (Lee and Terzopoulos, 2008)), we can in principle achieve similar animation results through equivalent joint-torque-driven simulation. The accompanying video includes a comparison of our muscle-actuated simulation against both inverse-dynamic (ID) and PD joint-torque actuated simulation. In the case of swimming, we obtained plausible results using joint-torque actuation, but it was necessary to set high gains for the PD joint-torque controllers accompanied with an order-of-magnitude smaller numerical time-step compared to the muscle-based approach. Moreover, a further advantage of the latter is that modifying the parameters of contractile muscles situated in anatomically accurate positions is the natural way to create nuanced biological motion patterns, including pathological ones (Wang et al., 2012), as well as of naturally effecting realistic flesh deformations (Lee et al., 2009).

7.3 Flesh Simulation vs. Procedural Skinning

On a fundamental level, we advocate volumetric soft-tissue simulation as this is the principled fleshing approach from a biological perspective. However, procedural skinning techniques have traditionally been more familiar to graphics practitioners. The accompanying video includes a comparison of our deformable flesh simulation against a state-of-the-art dual-quaternion skinning method (Kavan et al., 2008) with bounded biharmonic weights (Jacobson et al., 2011). The volumetric flesh simulation and procedural skinning result in similar swimming performances.

Experiment	Average Swimming Speed (m/s)
CPG muscle control	0.973
Spline muscle control	0.956
ID joint control	0.954
PD joint control	0.889
Simple skinning	0.916
Simple fluid model	0.614

Table 7.1: Average speed of the virtual swimmer in various experimental scenarios.

From some but not all viewpoints, the skin deformation appears plausible as the body articulates, but it cannot adequately synthesize anatomically detailed deformations, such as the muscle bulging effects demonstrated in Figure 6.8.

7.4 Fluid Simulation vs. Velocity Fields

On a fundamental level, we advocate a detailed physical simulation of the swimmer's environment, particularly Navier-Stokes simulation of water. However, procedural velocity field techniques have traditionally been easier for graphics practitioners to use (c.f. (Tu and Terzopoulos, 1994)). The accompanying video includes a comparison of the use of our water simulation approach against the use of a static, zero-velocity water field, employing the same flesh-water force coupling method for both. With the same amount of muscle effort, the virtual swimmer swims significantly faster in the simulated fluid environment compared to the zero-velocity field. Moreover, fluid simulation provides realistic wave, splash, and other effects that are entirely absent with the latter.

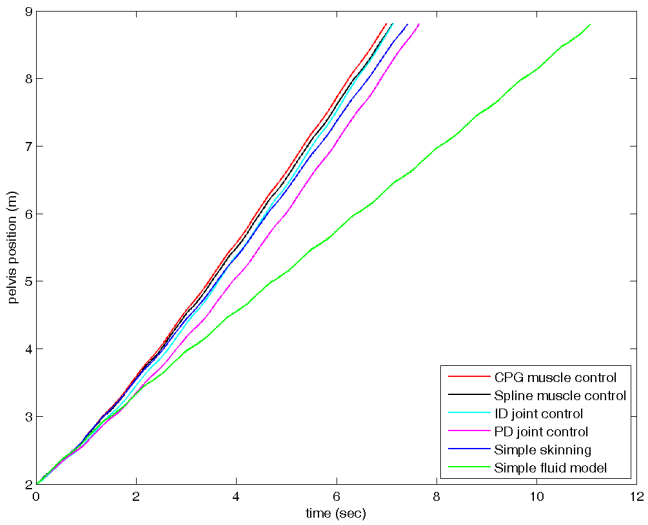

Figure 7.1: Comparison of swimming performance in various experimental scenarios.

7.5 A Comparison of Swimming Performances

Figure 7.1 presents a quantitative comparison of the performance of our virtual swimmer in the experimental scenarios described in the previous sections of this appendix, by plotting the distance traveled by the swimmer's pelvis over time. The table in Figure 7.1 indicates the associated average swimming speeds. In the figure and table, *CPG muscle control* refers to our experimental setting developed in the main text of this paper—i.e. using CPG locomotion control to synthesize muscle-length signals for the muscle-driven biomechanical body simulation with simulated flesh situated in simulated water. Under this same simulation scenario, *spline muscle control* refers to the use of B-splines to synthesize the muscle-length signals (Section 7.1), *ID joint control* refers to inverse-dynamics controlled joint-torque driven simulation (Section 7.2), and *PD joint control* refers to PD-controlled joint-torque driven simulation (Section 7.2). *Simple skinning* refers to using the dual quaternion skinning approach (Section 7.3). *Simple fluid model* refers to using a zero-velocity field (Section 7.4).

The figure and table reveal that the virtual swimmer swims most efficiently in our original experimental scenario. The swimmer can achieve similar swimming performances in the other experimental settings, except when the simulated fluid model is replaced by a zero-velocity field, which result in significantly lower efficiency.

CHAPTER 8

Conclusion

8.1 Contributions of the Thesis

In summary, the primary contributions of the human animation research reported in this dissertation are as follows:

- We have introduced **a multiphysics simulation and control framework** within whose scope is the realistic animation of a sophisticated autonomous human model that is capable of controlled swimming and underwater orientation control.

- We have developed **a comprehensive biomechanical model of the human body**, which includes 103 rigid bones (comprising 163 articular degrees of freedom) simulated as an articulated, multibody dynamical system that is driven by 823 muscles modeled as piecewise uniaxial Hill-type contractile actuators, plus a muscle and passive flesh simulation via an efficient volumetric finite element model of quasi-incompressible elastic material augmented with active (contractile) muscle terms, as well as the appropriate two-way coupling between the articulated skeleton and deformable flesh.

- With regard to **the control of the biomechanical human model** to synthesize complex, coordinated movements in water, we developed a Central Pattern Generator (CPG) based controller that generates muscle activation signals to induce appropriately coordinated muscle contractions. We also

developed a multiobjective optimization based control method that enables our biomechanical human model to accomplish nonperiodic, task-oriented motions in water while encouraging motion naturalness and avoiding self-collisions.

8.2 Future Work

Contemplating how people learn to swim, we are inspired to further investigate this topic in our future work. Humans learn to swim by first learning the movement of the limbs, perhaps by mimicking swimming demonstrations. This corresponds to the supervised learning process of our CPG system. After attaining command of the kinematic pattern of a swimming stroke, one can improve one's swimming skill through practice. This can be treated as an optimization process. As seen in the video, currently the motions of our swimmer are not very efficient, but we can try to optimize the learned parameters of our CPG system in order to improve efficiency. Generally speaking, CPG models offer a good substrate for automated learning and optimization algorithms. Studying how the swimmer responds to perturbations will be another interesting research direction. We can potentially simulate how a human should perform swimming in a torrential flow.

In the aquatic environment, we do not deal with balance, and losing balance does not cause serious problems for underwater motion control in a calm water environment, since buoyancy approximately cancels gravity and humans can efficiently control their limbs to generate proper drag forces, thus making their motions controllable. Under large perturbations, however, we are forced to confront balance in order to produce controllable motion. Balance is also a very troublesome issue when controlling terrestrial motion. It will not suffice to simply apply our CPG controller to walking and running motions as we would need to develop a more sophisticated feedback scheme to handle the balance problem.

This will be another interesting avenue for future work. Real world motion may be a superimposition of locomotion and voluntary movements; e.g., waving hands while walking. Combining our CPG controller with other controllers, such as the neuromuscular controller developed in (Lee and Terzopoulos, 2006), may be a viable approach to dealing with a broader variety of motor tasks.

For our orientation controller, the motion efficiency and naturalness are still not up to the standards of real human motion. Motion efficiency can be improved by formulating a better objective function for changing orientation, as well as a better approximation of the net hydrodynamic force effect. GP approaches have shown promise in synthesising natural kinematic human motion, and another possible direction for future work is finding a better way to couple the task control with the GP to improve the motion naturalness while not losing motion efficiency.

Energy efficiency, which is an important principle for human motion, is not considered in our proposed controllers. Since we cannot afford global spatiotemporal optimization for our complex system, it is very challenging to apply the energy efficiency principle to the system directly. A possible solution is to obtain an energy-efficient controller from a simplified system and then refine it for use in the actual simulation framework, another possible avenue for future work.

APPENDIX A

Rendering

We use the open-source POV-Ray software to render our simulation results. The geometries of the skin, muscles, and skeleton are embedded into the hexahedra of the embedding volume. This embedding framework preserves high resolution geometry for rendering. The water is treated as an isosurface object. The particle level set method provides a level set representation for the surface of the water, however, this level set representation cannot generate rich splashing effects unless the fluid is simulated at very high resolution. To make our fluid simulation affordable and the rendering result visually appealing, we make use of a byproduct of the fluid simulation, the removed negative particles, to render splashes.

We reconstruct a smooth surface representation from the removed negative particles using the approach in (Yu and Turk, 2010), which formulates the implicit surface representation as a sum of anisotropic smoothing kernels. The direction of anisotropy at a particle is determined by performing Principal Components Analysis (PCA) over the neighboring particles. Since these anisotropic smoothing kernels capture the local particle distributions more accurately, this method has advantages in representing smooth surfaces, thin streams, and sharp fluid features. It is also fast and easy to implement.

The surface is defined as an isosurface of a scalar field

$$\phi(\mathbf{x}) = \sum_j \frac{m_j}{\rho_j} W(\mathbf{x} - \mathbf{x}_j, \mathbf{G}_j), \tag{A.1}$$

where $\mathbf{x}$ is a location in space, m_j is the particle mass, and W is an anisotropic

smoothing kernel of the form

$$W(\mathbf{r}, \mathbf{G}) = \sigma \|\mathbf{G}\| P(\|\mathbf{G}\mathbf{r}\|). \tag{A.2}$$

Here, $\mathbf{r}$ is a radial vector, $\mathbf{G}$ is a linear transformation that rotates and stretches $\mathbf{r}$, σ is a scaling factor, which we set to $-\frac{315}{65\pi}$, and P is a symmetric decaying spline with finite support, which we simply define P as

$$P(x) = \begin{cases} (1-x)^3 & \text{if } 0 \le x \le 1 \\ 0 & \text{otherwise.} \end{cases} \tag{A.3}$$

The density ρ_i in (A.1) is interpolated by a sum of the weighted contributions of nearby particle masses m_j:

$$\rho_i = \sum_j m_j W(\mathbf{x}_j - \mathbf{x}_i, \mathbf{G}_j). \tag{A.4}$$

The key idea of this method is to associate an anisotropic matrix $\mathbf{G}_j$ with each particle j so that $\mathbf{G}_j$ more accurately represents the neighborhood density distribution. In order to determine $\mathbf{G}$, we apply the weighted version of PCA (WPCA) that is proposed in (Koren and Carmel, 2003) to the neighborhood particle positions. Specifically, WPCA begins by computing a weighted mean of data points:

$$\mathbf{x}_i^w = \sum_j w_{ij} \mathbf{x}_j / \sum_j w_{ij}. \tag{A.5}$$

Next, it constructs a weighted covariance matrix $\mathbf{C}$ with a zero empirical mean:

$$\mathbf{C}_i = \sum_j w_{ij} (\mathbf{x}_j - \mathbf{x}_i^w) (\mathbf{x}_j - \mathbf{x}_i^w)^T / \sum_j w_{ij}. \tag{A.6}$$

The function w_{ij} is an isotropic weighting function with respect to particle i and j with support r_i:

$$w_{ij} = \begin{cases} 1 - (\|\mathbf{x}_i - \mathbf{x}_j\| / r_i)^3 & \text{if } \|\mathbf{x}_i - \mathbf{x}_j\| < r_i, \\ 0 & \text{otherwise.} \end{cases} \tag{A.7}$$

With the finite support of w_{ij}, the computation is confined to the neighborhood particles within the radius r_i. To determine efficiently the particles that are within some radius of each particle, we build a balanced k-d tree for all the particles ahead of the other computations.

Then we perform an eigendecomposition on $\mathbf{C}$:

$$\mathbf{C} = \mathbf{R}\Sigma\mathbf{R}^T, \tag{A.8}$$

where $\mathbf{R}$ is a rotation matrix with principal axes as column vectors, and Σ is a diagonal matrix with eigenvalues $\sigma_1 \geq \cdots \geq \sigma_d$:

$$\Sigma = \mathrm{diag}\left(\sigma_1, \cdots, \sigma_d\right). \tag{A.9}$$

In order to deal with singular matrices and prevent extreme deformations, we check if $\sigma_1 \geq k_r\sigma_d$ with a suitable positive constant $k_r > 1$. This condition is true when the largest variance in one principal axis is much bigger than the variance in another axis. In this case, we modify $\mathbf{C}$ so that the ratio between any two eigenvalues is within k_r. When the number of particles in the neighborhood is too small, we reset W to a spherical shape by setting $\mathbf{G} = k_n\mathbf{I}$ in order to avoid poor particle deformations for nearly isolated particles. We also multiply $\mathbf{C}$ by scaling factor k_s such that $\|k_s\mathbf{C}\| \approx 1$ for the associated particle inside the fluid volume.

$$\widetilde{\Sigma} = \begin{cases} k_s\mathrm{diag}\left(\sigma_1, \widetilde{\sigma}_2, \cdots, \widetilde{\sigma}_d\right) & \text{if } N > N_\epsilon, \\ k_n\mathbf{I} & \text{otherwise,} \end{cases} \tag{A.10}$$

where $\widetilde{\sigma}_k = \max\left(\sigma_k, \sigma_1/k_r\right)$. In our application, we use $k_r = 4$, $k_s = 1400$, $k_n = 0.2$, and $N_\epsilon = 25$.

$$\mathbf{G}_i = \frac{1}{h_i}\mathbf{R}\widetilde{\Sigma}^{-1}\mathbf{R}^T. \tag{A.11}$$

We use $h_i = 0.04$ and $r_i = 2h_i$.

APPENDIX B

Improved Flesh-Bone Coupling

The key idea in improving flesh-bone coupling is to provide the Jacobian matrix of the attachment spring forces $\mathbf{f}_c$ with respect to the joint coordinates $\mathbf{q}$; i.e., $\frac{\partial \mathbf{f}_c}{\partial \mathbf{q}}$, so that we can take it into account in applying the implicit integration when performing the multibody dynamics simulation for the skeleton.

We define the quasistatic positions of nodes and attachments as follows:

$$\mathbf{x} = \begin{pmatrix} \mathbf{x}_u \\ \mathbf{x}_c \end{pmatrix}, \tag{B.1}$$

where $\mathbf{x}_u$ are the quasistatic positions of the nodes and $\mathbf{x}_c$ are the quasistatic positions of the attachment points. Figure B.1 provides a 2D interpretation, where $\mathbf{x}_u$ are indicated as blue dots and $\mathbf{x}_c$ as black dots.

Since the attachment points are obtained by sampling the bone surface, $\mathbf{x}_c$ are entirely determined by the skeleton configuration, and we have

$$\mathbf{x}_c = \mathbf{x}_c(\mathbf{q}), \tag{B.2}$$

where $\mathbf{q}$ are the joint coordinates. It is easy to compute the $\frac{\partial \mathbf{x}_c}{\partial \mathbf{q}}$.

After the deformable flesh is computed for a quasi-static equilibrium configuration, the net elastic forces acting on the nodes are $\mathbf{0}$; i.e.,

$$\mathbf{f}_u\left(\mathbf{x}_u, \mathbf{x}_c\right) = \mathbf{0} \tag{B.3}$$

The partial derivatives of $\mathbf{f}_u$ with respect to $\mathbf{q}$ is also null:

$$\frac{\partial}{\partial \mathbf{q}} \mathbf{f}_u\left(\mathbf{x}_u, \mathbf{x}_c\right) = \mathbf{0} \tag{B.4}$$

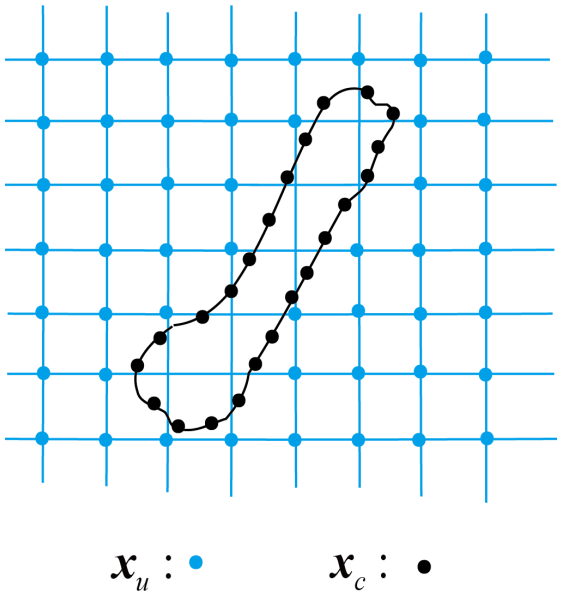

Figure B.1: A 2D interpretation of the nodes and attachment points. The nodes $\mathbf{x}_u$ *are denoted as blue dots. The attachment points* $\mathbf{x}_c$ *are denoted as black dots.*

Applying the chain rule to (B.4), we have

$$\frac{\partial \mathbf{f}_u}{\partial \mathbf{x}_u}\frac{\partial \mathbf{x}_u}{\partial \mathbf{q}} + \frac{\partial \mathbf{f}_u}{\partial \mathbf{x}_c}\frac{\partial \mathbf{x}_c}{\partial \mathbf{q}} = \mathbf{0}. \tag{B.5}$$

Since the flesh is coupled to the bone through zero natural-length springs, $\mathbf{x}_c$ contributes a linear part to $\mathbf{f}_u$, and we have

$$\frac{\partial \mathbf{f}_u}{\partial \mathbf{x}_c} = \mathbf{K}, \tag{B.6}$$

where $\mathbf{K}$ is the stiffness matrix. Since the elastic force can be expressed as the negative gradient of the potential energy E, we have

$$\mathbf{f}_u = -\frac{\partial E}{\partial \mathbf{x}_u}. \tag{B.7}$$

Computing the partial derivatives with respect to $\mathbf{x}_u$ on both sides gives us

$$-\frac{\partial \mathbf{f}_u}{\partial \mathbf{x}_u} = \frac{\partial^2 E}{\partial x_u^2}. \tag{B.8}$$

We can solve for $\frac{\partial \mathbf{x}_u}{\partial \mathbf{q}}$ according to (B.5).

Since the spring forces on the attachment points are $\mathbf{f}_c = \mathbf{f}_c(\mathbf{x}_u, \mathbf{x}_c)$, we have

$$\frac{\partial \mathbf{f}_c}{\partial \mathbf{q}} = \frac{\partial \mathbf{f}_c}{\partial \mathbf{x}_u}\frac{\partial \mathbf{x}_u}{\partial \mathbf{q}} + \frac{\partial \mathbf{f}_c}{\partial \mathbf{x}_c}\frac{\partial \mathbf{x}_c}{\partial \mathbf{q}}. \tag{B.9}$$

Since both $\mathbf{x}_u$ and $\mathbf{x}_c$ contribute linearly to $\mathbf{f}_c$, we can easily compute $\frac{\partial \mathbf{f}_c}{\partial \mathbf{x}_u}$ and $\frac{\partial \mathbf{f}_c}{\partial \mathbf{x}_c}$, while $\frac{\partial \mathbf{x}_c}{\partial \mathbf{q}}$ and $\frac{\partial \mathbf{x}_u}{\partial \mathbf{q}}$ are already computed above, and we can compute $\frac{\partial \mathbf{f}_c}{\partial \mathbf{q}}$ according to (B.9).

APPENDIX C

Derivatives of B-splines

Given m real valued knots t_i, with $t_0 \leq t_1 \leq \cdots \leq t_{m-1}$, a B-spline of degree n is a parametric curve

$$C : [t_n, t_{m-n-1}] \to \mathbb{R} \tag{C.1}$$

composed of a linear combination of basis B-splines $N_{i,n}$ of degree n:

$$C(t) = \sum_{i=0}^{m-n-2} P_i N_{i,n}(t). \tag{C.2}$$

The points $P_i \in \mathbb{R}$ are control points. The $m - n - 1$ basis B-splines of degree n can be defined using the following recursion formula:

$$N_{j,0}(t) = \begin{cases} 1, & \text{if } t_j \leq t < t_{j+1},\ j = 0, ..., m-2. \\ 0, & \text{otherwise,} \end{cases} \tag{C.3}$$

$$N_{j,n}(t) = \frac{t - t_j}{t_{j+n} - t_j} N_{j,n-1}(t) + \frac{t_{j+n+1} - t}{t_{j+n+1} - t_{j+1}} N_{j+1,n-1}(t), \qquad j = 0, ..., m-n-2. \tag{C.4}$$

The first and second order derivatives of the basis B-splines can be computed as follows:

$$\frac{d}{dt} N_{i,n}(t) = \frac{n}{t_{i+n} - t_i} N_{i,n-1}(t) - \frac{n}{t_{i+n-1} - t_{n+1}} N_{i+1,n-1}(t); \tag{C.5}$$

$$
\begin{aligned}
\frac{d^2}{dt^2}N_{i,n}(t) &= \frac{n}{t_{i+n}-t_i}\frac{d}{dt}N_{i,n-1}(t) - \frac{n}{t_{i+n+1}-t_{i+1}}\frac{d}{dt}N_{i+1,n-1}(t) \\
&= \frac{n}{t_{i+n}-t_i}\left(\frac{n-1}{t_{i+n-1}-t_i}N_{i,n-2}(t) - \frac{n-1}{t_{i+n}-t_{i+1}}N_{i+1,n-2}(t)\right) \\
&\quad - \frac{n}{t_{i+n+1}-t_{i+1}}\left(\frac{n-1}{t_{i+n}-t_{i+1}}N_{i+1,n-2}(t) - \frac{n-1}{t_{i+n+1}-t_{i+2}}N_{i+2,n-2}(t)\right) \\
&= n(n-1)\left(\frac{N_{i,n-2}(t)}{(t_{i+n}-t_i)(t_{i++n-1}-t_i)} - \left(\frac{1}{(t_{i+n}-t_i)(t_{i+n}-t_{i+1})}\right.\right. \\
&\quad \left.\left. + \frac{1}{(t_{i+n+1}-t_{i+1})(t_{i+n}-t_{i+1})}\right)N_{i+1,n-2}(t) + \frac{N_{i+2,n-2}(t)}{(t_{i+n+1}-t_{i+1})(t_{i+n+1}-t_{i+2})}\right)
\end{aligned}
\tag{C.6}
$$

So for the B-spline $C(t)$, we can compute its first and second order derivatives as follows:

$$
\begin{aligned}
\frac{dC(t)}{dt} &= \sum_{i=0}^{m} P_i \frac{d}{dt}N_{i,n}(t) \\
&= \sum_{i=0}^{m} P_i \left(\frac{n}{t_{i+n}-t_i}N_{i,n-1}(t) - \frac{n}{t_{i+n+1}-t_{i+1}}N_{i+1,n-1}(t)\right) \\
&= P_0\frac{n}{t_n-t_0}N_{0,n-1}(t) + \sum_{i=1} m(P_i - P_{i-1})\frac{n}{t_{n+i}-t_i}N_{i,n-1}(t) \\
&\quad - P_m\frac{n}{t_{m+n+1}-t_{m+1}}N_{m+1,n-1}(t)
\end{aligned}
\tag{C.7}
$$

$$
\begin{aligned}
\frac{d^2C(t)}{dt^2} &= \sum_{i=0}^{m} P_i \frac{d^2}{dt^2}N_{i,n}(t) \\
&= n(n-1)\left(N_{0,n-2}(t)\frac{P_0}{(t_n-t_0)(t_{n-1}-t_0)}\right. \\
&\quad + N_{1,n-2}(t)\left(-\frac{P_0}{(t_n-t_0)(t_n-t_1)} - fracP_0 - P_1(t_{n+1}-t_1)(t_n-t_1)\right) \\
&\quad + \sum_{i=2}^{m} N_{i,n-2}(t)\left(\frac{P_{i-2}-P_{i-1}}{(t_{i+n-1}-t_{i-1})(t_{i+n-1}-t_i)} - \frac{P_{i-1}-P_i}{(t_{i+n}-t_i)(t_{i+n-1}-t_i)}\right) \\
&\quad + N_{m+1,n-2}(t)\left(\frac{P_{m-1}-P_m}{(t_{m+n}-t_m)(t_{m+n}-t_{m+1})} - \frac{P_m}{(t_{m+n+1}-t_{m+1})(t_{m+n}-t_{m+1})}\right) \\
&\quad \left. + N_{m+2,n-2}(t)\frac{P_m}{(t_{m+n+1}-t_{m+1})(t_{m+n+1}-t_{m+2})}\right)
\end{aligned}
\tag{C.8}
$$

APPENDIX D

Gaussian Process Dynamical Model Details

In order to characterize natural human motion, we train GPDMs using motion capture data of a human swinging his arms and legs. Given the learned model $\Gamma = \{\mathbf{Y}, \mathbf{X}, \bar{\alpha}, \bar{\beta}, \mathbf{W}\}$, the distribution over a new sequence $\hat{\mathbf{Y}}$ and its associated latent trajectory $\hat{\mathbf{X}}$ is given by

$$p\left(\hat{\mathbf{Y}}, \hat{\mathbf{X}}|\Gamma\right) = p\left(\hat{\mathbf{Y}}|\hat{\mathbf{X}}, \Gamma\right) p\left(\hat{\mathbf{X}}|\Gamma\right). \tag{D.1}$$

Here, $\mathbf{Y} \equiv [\mathbf{y}_1, \cdots, \mathbf{y}_N]^T$ are the observations (training data) and $\mathbf{y}_1, \cdots, \mathbf{y}_N$ is a sequence of observed feature vectors. In our application, we use joint angles as the feature vector. $\mathbf{X} \equiv [\mathbf{x}_1, \cdots, \mathbf{x}_N]^T$ are the corresponding latent coordinates. Let D be the dimension of the feature vector $\mathbf{y}$, d the dimension of the latent vector $\mathbf{x}$, and $W = \text{diag}\,(w_1, \cdots, w_D)$ be a $D \times D$ diagonal scaling matrix. We use two previous frames to infer a new pose—i.e. we use the poses in frame $n-1$ and frame n to infer the new pose in frame $n+1$. Thus, we have $\hat{\mathbf{Y}} = [\hat{\mathbf{y}}_{n-1}, \hat{\mathbf{y}}_n, \hat{\mathbf{y}}_{n+1}]^T$, $\hat{\mathbf{X}} = [\hat{\mathbf{x}}_{n-1}, \hat{\mathbf{x}}_n, \hat{\mathbf{x}}_{n+1}]^T$. The distribution of $p\left(\hat{\mathbf{Y}}|\hat{\mathbf{X}}, \Gamma\right)$ is Gaussian and it can be written as follows:

$$p\left(\hat{\mathbf{Y}}|\hat{\mathbf{X}}, \Gamma\right) = \frac{|\mathbf{W}|^M}{\sqrt{(2\pi)^{MD}\,|\mathbf{K}(\hat{\mathbf{X}})|^D}} \exp\left(-\frac{1}{2}\text{tr}\left(\mathbf{K}^{-1}(\hat{\mathbf{X}})\mathbf{Z}_Y\mathbf{W}^2\mathbf{Z}_Y^T\right)\right), \tag{D.2}$$

where M is the number of feature vectors in the new sequence; in our application $M = 3$. We use the RBF kernel to define a kernel k_Y as

$$k_Y(\mathbf{x}, \mathbf{x}') = \exp\left(-\frac{\beta_1}{2}\|\mathbf{x} - \mathbf{x}'\|^2\right) + \beta_2^{-1}\delta_{\mathbf{x},\mathbf{x}'}, \tag{D.3}$$

Now,

$$\mathbf{Z}_Y = \hat{\mathbf{Y}} - \mathbf{K}_{\hat{\mathbf{X}},\mathbf{X}}\mathbf{K}_Y^{-1}\mathbf{Y}, \tag{D.4}$$

and

$$\mathbf{K}(\hat{\mathbf{X}}) = \mathbf{K}_{\hat{\mathbf{X}},\hat{\mathbf{X}}} - \mathbf{K}_{\hat{\mathbf{X}},\mathbf{X}}\mathbf{K}_Y^{-1}\mathbf{K}_{\hat{\mathbf{X}},\mathbf{X}}^T, \tag{D.5}$$

where

$$\mathbf{K}_{\hat{\mathbf{X}},\hat{\mathbf{X}}} = \begin{pmatrix} k_Y(\hat{\mathbf{x}}_{n-1},\hat{\mathbf{x}}_{n-1}) & k_Y(\hat{\mathbf{x}}_{n-1},\hat{\mathbf{x}}_n) & k_Y(\hat{\mathbf{x}}_{n-1},\hat{\mathbf{x}}_{n+1}) \\ k_Y(\hat{\mathbf{x}}_n,\hat{\mathbf{x}}_{n-1}) & k_Y(\hat{\mathbf{x}}_n,\hat{\mathbf{x}}_n) & k_Y(\hat{\mathbf{x}}_n,\hat{\mathbf{x}}_{n+1}) \\ k_Y(\hat{\mathbf{x}}_{n+1},\hat{\mathbf{x}}_{n-1}) & k_Y(\hat{\mathbf{x}}_{n+1},\hat{\mathbf{x}}_n) & k_Y(\hat{\mathbf{x}}_{n+1},\hat{\mathbf{x}}_{n+1}) \end{pmatrix} \tag{D.6}$$

and

$$\mathbf{K}_{\hat{\mathbf{X}},\mathbf{X}} = \begin{pmatrix} k_Y(\hat{\mathbf{x}}_{n-1},\mathbf{x}_1) & k_Y(\hat{\mathbf{x}}_{n-1},\mathbf{x}_2) & \cdots & k_Y(\hat{\mathbf{x}}_{n-1},\mathbf{x}_N) \\ k_Y(\hat{\mathbf{x}}_n,\mathbf{x}_1) & k_Y(\hat{\mathbf{x}}_n,\mathbf{x}_2) & \cdots & k_Y(\hat{\mathbf{x}}_n,\mathbf{x}_N) \\ k_Y(\hat{\mathbf{x}}_{n+1},\mathbf{x}_1) & k_Y(\hat{\mathbf{x}}_{n+1},\mathbf{x}_2) & \cdots & k_Y(\hat{\mathbf{x}}_{n+1},\mathbf{x}_N) \end{pmatrix}. \tag{D.7}$$

The elements of the kernel matrix $\mathbf{K}_Y$ are defined by a kernel function $(\mathbf{K}_Y)_{ij} \equiv k_Y(\mathbf{x}_i, \mathbf{x}_j)$. Matrix $\mathbf{K}_Y$ need only be inverted once by using the learned model.

The distribution $p\left(\hat{\mathbf{X}}|\Gamma\right)$ is not Gaussian, but it can be expressed similar to (D.2):

$$p\left(\hat{\mathbf{X}}|\Gamma\right) = \frac{p\left(\hat{\mathbf{x}}_{n-1}\right)}{\sqrt{(2\pi)^{(M-1)d}}} \exp\left(-\frac{1}{2}\mathrm{tr}\left(\mathcal{K}^{-1}(\hat{\mathbf{X}}_{in})\mathbf{Z}_X\mathbf{Z}_X^T\right)\right). \tag{D.8}$$

We use a "linear + RBF" kernel to define a kernel k_X as follows:

$$k_X(\mathbf{x},\mathbf{x}') = \alpha_1 \exp\left(-\frac{\alpha_2}{2}\|\mathbf{x}-\mathbf{x}'\|^2\right) + \alpha_3\mathbf{x}^T\mathbf{x}' + \alpha_4^{-1}\delta_{\mathbf{x},\mathbf{x}'}. \tag{D.9}$$

Now,

$$\mathbf{Z}_X = \hat{\mathbf{X}}_{out} - \mathcal{K}_{\hat{\mathbf{X}}_{in},\mathbf{X}_{in}}\mathcal{K}_X^{-1}\mathbf{X}_{out} \tag{D.10}$$

$$\mathcal{K}\left(\hat{\mathbf{X}}_{in}\right) = \mathcal{K}_{\hat{\mathbf{X}}_{in},\hat{\mathbf{X}}_{in}} - \mathcal{K}_{\hat{\mathbf{X}}_{in},\mathbf{X}_{in}}\mathcal{K}_X^{-1}\mathcal{K}_{\hat{\mathbf{X}}_{in},\mathbf{X}_{in}}^T. \tag{D.11}$$

where

$$\mathbf{X}_{in} = \left[\mathbf{x}_1, \cdots, \mathbf{x}_{N-1}\right]^T, \tag{D.12}$$

$$\mathbf{X}_{out} = \left[\mathbf{x}_2, \cdots, \mathbf{x}_N\right]^T, \tag{D.13}$$

$$\hat{\mathbf{X}}_{in} = \left[\hat{\mathbf{x}}_{n-1}, \hat{\mathbf{x}}_n\right]^T, \tag{D.14}$$

$$\hat{\mathbf{X}}_{out} = \left[\hat{\mathbf{x}}_n, \hat{\mathbf{x}}_{n+1}\right]^T. \tag{D.15}$$

The elements of the kernel matrix $\mathcal{K}_X$ are defined by a kernel function $\left(\mathcal{K}_X\right)_{ij} \equiv k_X\left(\mathbf{x}_i, \mathbf{x}_j\right)$ constructed from $\mathbf{X}_{in}$, and $\mathcal{K}_{\hat{\mathbf{X}}_{in},\hat{\mathbf{X}}_{in}}$, and $\mathcal{K}_{\hat{\mathbf{X}}_{in},\mathbf{X}_{in}}$ are defined similarly. Matrix $\mathcal{K}_X$ also needs only be inverted once by using the learned model.

Conditional Likelihood and Related Derivatives

The likelihood of a sequence with three feature vectors $\hat{\mathbf{Y}}$ and the corresponding latent positions $\hat{\mathbf{X}}$ is computed as

$$L_S(\hat{\mathbf{Y}}, \hat{\mathbf{X}}) = L_Y(\hat{\mathbf{Y}}, \hat{\mathbf{X}}) + L_X(\hat{\mathbf{X}}), \tag{D.16}$$

where

$$L_Y(\hat{\mathbf{Y}}, \hat{\mathbf{X}}) = \frac{D}{2} \ln |\mathbf{K}(\hat{\mathbf{X}})| + \frac{1}{2}\mathrm{tr}\left(\mathbf{K}^{-1}(\hat{\mathbf{X}})\mathbf{Z}_Y\mathbf{W}^2\mathbf{Z}_Y^T\right) \tag{D.17}$$

and

$$L_X(\hat{\mathbf{X}}) = \frac{d}{2} \ln |\mathcal{K}(\hat{\mathbf{X}}_{in})| + \frac{1}{2}\mathrm{tr}\left(\mathcal{K}^{-1}(\hat{\mathbf{X}}_{in})\mathbf{Z}_X\mathbf{Z}_X^T\right). \tag{D.18}$$

Here, we also provide the partial derivatives of L_S:

$$\frac{\partial L_S}{\partial \hat{\mathbf{y}}_{n+1}} = \frac{\partial L_Y}{\partial \mathbf{Z}_Y}\frac{\partial \mathbf{Z}_Y}{\partial \hat{\mathbf{y}}_{n+1}}, \tag{D.19}$$

$$\frac{\partial L_S}{\partial \hat{\mathbf{x}}_{n+1}} = \frac{\partial L_Y}{\partial \mathbf{K}(\hat{\mathbf{X}})}\frac{\partial \mathbf{K}(\hat{\mathbf{X}})}{\partial \hat{\mathbf{x}}_{n+1}} + \frac{\partial L_Y}{\partial \mathbf{Z}_Y}\frac{\partial \mathbf{Z}_Y}{\partial \hat{\mathbf{x}}_{n+1}} + \frac{\partial L_X}{\partial \mathbf{Z}_X}\frac{\partial \mathbf{Z}_X}{\partial \hat{\mathbf{x}}_{n+1}}. \tag{D.20}$$

In greater detail,

$$\frac{\partial L_Y}{\partial \mathbf{K}(\hat{\mathbf{X}})} = \frac{D}{2}\mathbf{K}^{-1}(\hat{\mathbf{X}}) - \frac{1}{2}\mathbf{K}^{-1}(\hat{\mathbf{X}})\mathbf{Z}_Y\mathbf{W}^2\mathbf{Z}_Y^T\mathbf{K}^{-1}(\hat{\mathbf{X}}), \tag{D.21}$$

$$\frac{\partial L_Y}{\partial \mathbf{Z}_Y} = \mathbf{K}^{-1}(\hat{\mathbf{X}})\mathbf{Z}_Y\mathbf{W}^2, \tag{D.22}$$

$$\frac{\partial L_X}{\partial \mathbf{Z}_X} = \mathcal{K}^{-1}(\hat{\mathbf{X}}_{in})\mathbf{Z}_X. \tag{D.23}$$

Using $\hat{x}_i^j$ to denote the j-th element of the latent vector $\hat{\mathbf{x}}_i$,

$$\frac{\partial \mathbf{K}(\hat{\mathbf{X}})}{\partial \hat{x}_{n+1}^j} = \frac{\partial \mathbf{K}_{\hat{\mathbf{X}},\hat{\mathbf{X}}}}{\partial \hat{x}_{n+1}^j} - \frac{\partial\left(\mathbf{K}_{\hat{\mathbf{X}},\mathbf{X}}\mathbf{K}_Y^{-1}\mathbf{K}_{\hat{\mathbf{X}},\mathbf{X}}^T\right)}{\partial \hat{x}_{n+1}^j}. \tag{D.24}$$

In greater detail,

$$\frac{\partial \mathbf{K}_{\hat{\mathbf{X}},\hat{\mathbf{X}}}}{\partial \hat{x}_{n+1}^j} = \begin{pmatrix} 0 & 0 & \frac{\partial k_Y(\hat{\mathbf{x}}_{n-1},\hat{\mathbf{x}}_{n+1})}{\partial \hat{x}_{n+1}^j} \\ 0 & 0 & \frac{\partial k_Y(\hat{\mathbf{x}}_{n},\hat{\mathbf{x}}_{n+1})}{\partial \hat{x}_{n+1}^j} \\ \frac{\partial k_Y(\hat{\mathbf{x}}_{n+1},\hat{\mathbf{x}}_{n-1})}{\partial \hat{x}_{n+1}^j} & \frac{\partial k_Y(\hat{\mathbf{x}}_{n+1},\hat{\mathbf{x}}_{n})}{\partial \hat{x}_{n+1}^j} & 0 \end{pmatrix}, \tag{D.25}$$

where

$$\frac{\partial k_Y(\hat{\mathbf{x}}_i,\hat{\mathbf{x}}_{n+1})}{\partial \hat{x}_{n+1}^j} = \frac{\partial k_Y(\hat{\mathbf{x}}_{n+1},\hat{\mathbf{x}}_i)}{\partial \hat{x}_{n+1}^j} = -\beta_1(\hat{x}_{n+1}^j - \hat{x}_i^j)\exp\left(-\frac{\beta_1}{2}\|\hat{\mathbf{x}}_i - \hat{\mathbf{x}}_{n+1}\|^2\right). \tag{D.26}$$

$$\frac{\partial\left(\mathbf{K}_{\hat{\mathbf{X}},\mathbf{X}}\mathbf{K}_Y^{-1}\mathbf{K}_{\hat{\mathbf{X}},\mathbf{X}}^T\right)}{\partial \hat{x}_{n+1}^j} = \sum_{i=1}^{N}\frac{\partial\left(\mathbf{K}_{\hat{\mathbf{X}},\mathbf{X}}\mathbf{K}_Y^{-1}\mathbf{K}_{\hat{\mathbf{X}},\mathbf{X}}^T\right)}{\partial k_Y(\hat{\mathbf{x}}_{n+1},\mathbf{x}_i)}\frac{\partial k_Y(\hat{\mathbf{x}}_{n+1},\mathbf{x}_i)}{\partial \hat{x}_{n+1}^j}, \tag{D.27}$$

where

$$\frac{\partial\left(\mathbf{K}_{\hat{\mathbf{X}},\mathbf{X}}\mathbf{K}_Y^{-1}\mathbf{K}_{\hat{\mathbf{X}},\mathbf{X}}^T\right)}{\partial k_Y(\hat{\mathbf{x}}_{n+1},\mathbf{x}_i)} = \mathbf{G}_i + \mathbf{G}_i^T \tag{D.28}$$

and

$$\mathbf{G}_i = \mathbf{E}_{3\times N}^{(3,i)} \mathbf{K}_Y^{-1} \mathbf{K}_{\hat{\mathbf{X}},\mathbf{X}}^T \tag{D.29}$$

Here, we use $\mathbf{E}_{3\times N}^{(3,i)}$ to denote a matrix whose elements are 0 except that the $(3,i)$ element is 1. Substituting (D.28) and (D.29) into (D.27), we have

$$\frac{\partial \left(\mathbf{K}_{\hat{\mathbf{X}},\mathbf{X}} \mathbf{K}_Y^{-1} \mathbf{K}_{\hat{\mathbf{X}},\mathbf{X}}^T \right)}{\partial \hat{x}_{n+1}^j} = \mathbf{H} + \mathbf{H}^T, \tag{D.30}$$

where

$$\mathbf{H} = \begin{pmatrix} 0 & 0 & \cdots & 0 \\ 0 & 0 & \cdots & 0 \\ \frac{\partial k_Y(\hat{\mathbf{x}}_{n+1},\mathbf{x}_1)}{\partial \hat{x}_{n+1}^j} & \frac{\partial k_Y(\hat{\mathbf{x}}_{n+1},\mathbf{x}_2)}{\partial \hat{x}_{n+1}^j} & \cdots & \frac{\partial k_Y(\hat{\mathbf{x}}_{n+1},\mathbf{x}_N)}{\partial \hat{x}_{n+1}^j} \end{pmatrix} \mathbf{K}_Y^{-1} \mathbf{K}_{\hat{\mathbf{X}},\mathbf{X}}^T. \tag{D.31}$$

Furthermore,

$$\frac{\partial \mathbf{Z}_Y}{\partial \hat{x}_{n+1}^j} = - \begin{pmatrix} 0 & 0 & \cdots & 0 \\ 0 & 0 & \cdots & 0 \\ \frac{\partial k_Y(\hat{\mathbf{x}}_{n+1},\mathbf{x}_1)}{\partial \hat{x}_{n+1}^j} & \frac{\partial k_Y(\hat{\mathbf{x}}_{n+1},\mathbf{x}_2)}{\partial \hat{x}_{n+1}^j} & \cdots & \frac{\partial k_Y(\hat{\mathbf{x}}_{n+1},\mathbf{x}_N)}{\partial \hat{x}_{n+1}^j} \end{pmatrix} \mathbf{K}_Y^{-1} \mathbf{Y}, \tag{D.32}$$

$$\frac{\partial \mathbf{Z}_Y}{\partial \hat{y}_{n+1}^j} = \mathbf{E}_{3\times D}^{(3,j)}, \tag{D.33}$$

and

$$\frac{\partial \mathbf{Z}_X}{\partial \hat{x}_{n+1}^j} = \mathbf{E}_{2\times d}^{(2,j)}. \tag{D.34}$$

Partial Derivatives of the Naturalness Objective

To solve the nonlinear optimization problem (5.20) efficiently, we must provide the partial derivative $\frac{\partial E_{nat}(\hat{\mathbf{x}}_{n+1})}{\partial \hat{\mathbf{x}}_{n+1}}$. We apply chain rule to (5.20) and obtain

$$\begin{aligned} \frac{\partial E_{nat}\left(\hat{\mathbf{x}}_{n+1}\right)}{\partial \hat{\mathbf{x}}_{n+1}} = & \frac{\partial E_{orient}\left(\dot{\mathbf{q}}\left(\mu_Y(\hat{\mathbf{x}}_{n+1})\right)\right)}{\partial \dot{\mathbf{q}}\left(\mu_Y(\hat{\mathbf{x}}_{n+1})\right)} \frac{\partial \dot{\mathbf{q}}\left(\mu_Y(\hat{\mathbf{x}}_{n+1})\right)}{\partial \mu_Y(\hat{\mathbf{x}}_{n+1})} \frac{\partial \mu_Y\left(\hat{\mathbf{x}}_{n+1}\right)}{\partial \hat{\mathbf{x}}_{n+1}} \\ & + w_{prior} \frac{\partial L_X(\hat{\mathbf{X}})}{\partial \hat{\mathbf{x}}_{n+1}} + 2 w_{smooth} \left(\mu_Y(\hat{\mathbf{x}}_{n+1}) - \mu_Y(\hat{\mathbf{x}}_n)\right)^T \frac{\partial \mu_Y\left(\hat{\mathbf{x}}_{n+1}\right)}{\partial \hat{\mathbf{x}}_{n+1}} \\ & + w_{confid} \frac{\partial \sigma_Y^2\left(\hat{\mathbf{x}}_{n+1}\right)}{\partial \hat{\mathbf{x}}_{n+1}}. \end{aligned} \tag{D.35}$$

Here, we provide the mean of the pose reconstruction GP

$$\mu_Y\left(\hat{\mathbf{x}}\right) = \mathbf{Y}^T \mathbf{K}_Y^{-1} \mathbf{k}_Y\left(\hat{\mathbf{x}}\right), \tag{D.36}$$

where

$$\mathbf{k}_Y\left(\hat{\mathbf{x}}\right) = \begin{pmatrix} k_Y\left(\mathbf{x}_1, \hat{\mathbf{x}}\right) \\ k_Y\left(\mathbf{x}_2, \hat{\mathbf{x}}\right) \\ \vdots \\ k_Y\left(\mathbf{x}_N, \hat{\mathbf{x}}\right) \end{pmatrix} \tag{D.37}$$

and the prediction variance of the reconstruction GP is

$$\sigma_Y^2\left(\hat{\mathbf{x}}\right) = k_Y\left(\hat{\mathbf{x}}, \hat{\mathbf{x}}\right) - \mathbf{k}_Y\left(\hat{\mathbf{x}}\right)^T \mathbf{K}_Y^{-1} \mathbf{k}_Y\left(\hat{\mathbf{x}}\right) \tag{D.38}$$

So,

$$\frac{\partial \mu_Y\left(\hat{\mathbf{x}}_{n+1}\right)}{\partial \hat{\mathbf{x}}_{n+1}} = \mathbf{Y}^T \mathbf{K}_Y^{-1} \frac{\partial \mathbf{k}_Y\left(\hat{\mathbf{x}}_{n+1}\right)}{\partial \hat{\mathbf{x}}_{n+1}} \tag{D.39}$$

and

$$\frac{\partial \sigma_Y^2\left(\hat{\mathbf{x}}_{n+1}\right)}{\partial \hat{\mathbf{x}}_{n+1}} = \frac{\partial k_Y\left(\hat{\mathbf{x}}_{n+1}, \hat{\mathbf{x}}_{n+1}\right)}{\partial \hat{\mathbf{x}}_{n+1}} - 2\mathbf{k}_Y\left(\hat{\mathbf{x}}_{n+1}\right)^T \mathbf{K}_Y^{-1} \frac{\partial \mathbf{k}_Y\left(\hat{\mathbf{x}}_{n+1}\right)}{\partial \hat{\mathbf{x}}_{n+1}} \tag{D.40}$$

since

$$\frac{\partial L_X(\hat{\mathbf{X}})}{\partial \hat{\mathbf{x}}_{n+1}} = \frac{\partial L_X}{\partial \mathbf{Z}_X} \frac{\partial \mathbf{Z}_X}{\partial \hat{\mathbf{x}}_{n+1}}, \tag{D.41}$$

where $\frac{\partial L_X}{\partial \mathbf{Z}_X}$ and $\frac{\partial \mathbf{Z}_X}{\partial \hat{\mathbf{x}}_{n+1}}$ are given in (D.23) and (D.34), respectively. Substituting (D.39), (D.40), and (D.41) into (D.35), we can compute $\frac{\partial E_{nat}(\hat{\mathbf{x}}_{n+1})}{\partial \hat{\mathbf{x}}_{n+1}}$.

Bibliography

Agache, P., Monneur, C., Leveque, J., and Rigal, J. (1980). Mechanical properties and Young's modulus of human skin in vivo. *Archives of Dermatological Research*, 269(3):221–232. 51

Albrecht, I., Haber, J., and Seidel, H.-P. (2003). Construction and animation of anatomically based human hand models. In *ACM SIGGRAPH/EG Symposium on Computer Animation (SCA'03)*, pages 98–109. 8

Benson, D. J. (1992). Computational methods in Lagrangian and Eulerian hydrocodes. *Comput. Methods Appl. Mech. Eng.*, 99:235–394. 26

de Boor, C. (1978). *A Practical Guide to Splines*. Springer-Verlag. 34

Dong, F., Clapworthy, G. J., Krokos, M. A., and Yao, J. (2002). An anatomy-based approach to human muscle modeling and deformation. *IEEE Transactions on Visualization and Computer Graphics*, 8(2):154–170. 8

Enright, D., Marschner, S., and Fedkiw, R. (2002). Animation and rendering of complex water surfaces. In *Proceedings of the 29th Annual Conference on Computer Graphics and Interactive Techniques*, SIGGRAPH '02, pages 736–744, New York, NY. ACM. 24, 25

Faloutsos, P., van de Panne, M., and Terzopoulos, D. (2001). Composable controllers for physics-based character animation. In *Proceedings of the 28th Annual Conference on Computer Graphics and Interactive Techniques*, SIGGRAPH '01, pages 251–260, New York, NY. ACM. 8

Featherstone, R. (1987). *Robot Dynamics Algorithms*. Kluwer Academic Publishers, Boston. 16, 17

Fedkiw, R. P. (2002). Coupling an Eulerian fluid calculation to a Lagrangian solid calculation with the ghost fluid method. *J. Comput. Phys.*, 175:200–224. 26

Foster, N. and Fedkiw, R. (2001). Practical animation of liquids. In *Proceedings of the 28th Annual Conference on Computer Graphics and Interactive Techniques*, SIGGRAPH '01, pages 23–30, New York, NY. ACM. 24, 25

Fung, Y. (1993). *Biomechanics: Mechanical Properties of Living Tissues*. Springer, New York, NY. 16

Gams, A., Ijspeert, A. J., Schaal, S., and Lenarcic, J. (2009). On-line learning and modulation of periodic movements with nonlinear dynamical systems. *Autonomous Robots*, 27(1):3–23. 35, 37

Gill, P., Murray, W., and Saunders, M. (2002). SNOPT: An SQP algorithm for large-scale constrained optimization. *SIAM Journal on Optimization*, 12(4):979–1006. 50

Grochow, K., Martin, S. L., Hertzmann, A., and Popović, Z. (2004). Style-based inverse kinematics. In *Proceedings of the ACM SIGGRAPH Conference*, SIGGRAPH '04, pages 522–531, New York, NY. ACM. 11

Grzeszczuk, R. and Terzopoulos, D. (1995). Automated learning of muscle-actuated locomotion through control abstraction. In *Proceedings of the ACM SIGGRAPH Conference*, Computer Graphics Proceedings, Annual Conference Series, pages 63–70. 9, 11, 40

Hase, K., Miyashita, K., Ok, S., and Arakawa, Y. (2003). Human gait simulation with a neuromusculoskeletal model and evolutionary computation. *The Journal of Visualization and Computer Animation*, 14(2):73–92. 10

Ho, E. S. L., Komura, T., and Tai, C.-L. (2010). Spatial relationship preserving character motion adaptation. In *Proceedings of the ACM SIGGRAPH Conference*, SIGGRAPH '10, pages 33:1–33:8, New York, NY. ACM. 49

Hodgins, J. K., Wooten, W. L., Brogan, D. C., and O'Brien, J. F. (1995). Animating human athletics. In *Proceedings of the 22nd Annual Conference on Computer Graphics and Interactive Techniques*, SIGGRAPH '95, pages 71–78, New York, NY. ACM. 8

Ijspeert, A. J. (2008). Central pattern generators for locomotion control in animals and robots: A review. *Neural Networks*, 21(4):642–653. 10

Ijspeert, A. J., Crespi, A., Ryczko, D., and Cabelguen, J.-M. (2007). From swimming to walking with a salamander robot driven by a spinal cord model. *Science*, 315(5817):1416–1420. 10

Ikemoto, L., Arikan, O., and Forsyth, D. (2009). Generalizing motion edits with Gaussian processes. *ACM Transactions on Graphics*, 28(1):1:1–1:12. 11

Jacobson, A., Baran, I., Popović, J., and Sorkine, O. (2011). Bounded biharmonic weights for real-time deformation. *ACM Transactions on Graphics (Proceedings of the ACM SIGGRAPH Conference)*, 30(4):78:1–78:8. 67

Kavan, L., Collins, S., Žára, J., and O'Sullivan, C. (2008). Geometric skinning with approximate dual quaternion blending. *ACM Transactions on Graphics*, 27(4):105. 67

Komura, T., Shinagawa, Y., and Kunii, T. L. (2000). Creating and retargetting motion by the musculoskeletal human body model. *The Visual Computer*, 16(5):254–270. 8

Koren, Y. and Carmel, L. (2003). Visualization of labeled data using linear transformations. In *Proceedings of the Ninth Annual IEEE Conference on Information Visualization*, INFOVIS'03, pages 121–128, Washington, DC. IEEE Computer Society. 75

Kwatra, N., Wojtan, C., Carlson, M., Essa, I., Mucha, P. J., and Turk, G. (2010). Fluid simulation with articulated bodies. *IEEE Transactions on Visualization and Computer Graphics*, 16:70–80. 9, 10

Lawrence, N. (2004). Gaussian process latent variable models for visualisation of high dimensional data. *Advances in Neural Information Processing Systems*, 16:329–336. 11

Lee, S.-H., Sifakis, E., and Terzopoulos, D. (2009). Comprehensive biomechanical modeling and simulation of the upper body. *ACM Transactions on Graphics*, 28:99:1–99:17. 8, 16, 19, 30, 40, 41, 42, 49, 67

Lee, S.-H. and Terzopoulos, D. (2006). Heads up! Biomechanical modeling and neuromuscular control of the neck. In *Proceedings of the ACM SIGGRAPH Conference*, SIGGRAPH '06, pages 1188–1198, New York, NY. ACM. 8, 73

Lee, S.-H. and Terzopoulos, D. (2008). Spline joints for multibody dynamics. *ACM Transactions on Graphics*, 27(3):22:1–22:8. 67

Lee, Y., Terzopoulos, D., and Waters, K. (1995). Realistic modeling for facial animation. In *Proceedings of ACM SIGGRAPH 95*, Computer Graphics Proceedings, Annual Conference Series, pages 55–62. 8

Lentine, M., Gretarsson, J. T., Schroeder, C., Robinson-Mosher, A., and Fedkiw, R. (2011). Creature control in a fluid environment. *IEEE Transactions on Visualization and Computer Graphics*, 17:682–693. 9, 11, 27

Levine, S., Wang, J. M., Haraux, A., Popović, Z., and Koltun, V. (2012). Continuous character control with low-dimensional embeddings. *ACM Transactions on Graphics*, 31(4):28. 11, 47, 48

Ljung, L. and Söderström, T. (1983). *Theory and Practice of Recursive Identification*. The MIT Press, Massachusetts and London. 37

MacKay-Lyons, M. (2002). Central pattern generation of locomotion: A review of the evidence. *Physical Therapy*, 82(1):69–83. 10

McAdams, A., Zhu, Y., Selle, A., Empey, M., Tamstorf, R., Teran, J., and Sifakis, E. (2011). Efficient elasticity for character skinning with contact and collisions. In *Proceedings of the ACM SIGGRAPH Conference*, SIGGRAPH '11, pages 37:1–37:12, New York, NY. ACM. 19, 30

Mukai, T. and Kuriyama, S. (2005). Geostatistical motion interpolation. In *Proceedings of the ACM SIGGRAPH Conference*, SIGGRAPH '05, pages 1062–1070, New York, NY. ACM. 11

Nakamura, Y., Yamane, K., Fujita, Y., and Suzuki, I. (2005). Somatosensory computation for man machine interface from motion-capture data and musculoskeletal human model. *IEEE Transactions on Robotics*, 21(1):58–66. 8

Orin, D. and Goswami, A. (2008). Centroidal momentum matrix of a humanoid robot: Structure and properties. In *Proceedings of the IEEE/RSJ International Conference on Intelligent Robots and Systems (IROS)*, pages 653 –659. 42

Patterson, T., Mitchell, N., and Sifakis, E. (2012). Simulation of complex nonlinear elastic bodies using lattice deformers. *ACM Transactions on Graphics*, 31(6):197:1–197:10. 19, 22

Righetti, L. and Ijspeert, A. J. (2006). Programmable central pattern generators: An application to biped locomotion control. In *Proceedings of the 2006 IEEE International Conference on Robotics and Automation*, pages 1585–1590. 10

Schaal, S. and Atkeson, C. G. (1997). Constructive incremental learning from only local information. *Neural Computation*, 10:2047–2084. 33

Sueda, S., Kaufman, A., and Pai, D. K. (2008). Musculotendon simulation for hand animation. *ACM Transactions on Graphics*, 27(3):83:1–83:8. 8

Taga, G. (1995). A model of the neuro-musculo-skeletal system for human locomotion. *Biological Cybernetics*, 73:113–121. 10

Tan, J., Gu, Y., Turk, G., and Liu, C. K. (2011). Articulated swimming creatures. In *Proceedings of the ACM SIGGRAPH Conference*, SIGGRAPH '11, pages 58:1–58:12, New York, NY. ACM. 9, 40

Thelen, D. G., Anderson, F. C., and Delp, S. L. (2003). Generating dynamic simulations of movement using computed muscle control. *Journal of Biomechanics*, 36(3):321–328. 40

Tsang, W., Singh, K., and Eugene, F. (2005). Helping hand: An anatomically accurate inverse dynamics solution for unconstrained hand motion. In *Proceedings of the 2005 ACM SIGGRAPH/EG Symposium on Computer Animation*, SCA '05, pages 319–328, New York, NY. ACM. 8

Tu, X. and Terzopoulos, D. (1994). Artificial fishes: Physics, locomotion, perception, behavior. In *Proceedings of the 21st Annual Conference on Computer Graphics and Interactive Techniques*, SIGGRAPH '94, pages 43–50, New York, NY. ACM. 9, 27, 68

Virtual-swim (2007). *Aquatic Animation for Analysis and Education*. `http://www.virtual-swim.com/`. 34

Wang, J. M., Fleet, D. J., and Hertzmann, A. (2008). Gaussian process dynamical models for human motion. *IEEE Transactions on Pattern Analysis and Machine Intelligence*, 30(2):283–298. 47

Wang, J. M., Hamner, S. R., Delp, S. L., and Koltun, V. (2012). Optimizing locomotion controllers using biologically-based actuators and objectives. *ACM Transactions on Graphics*, 31(4):25:1–25:11. Proceedings of the ACM SIGGRAPH Conference. 8, 67

Waters, K. (1987). A muscle model for animating three-dimensional facial expression. In *Proceedings of the 14th Annual Conference on Computer Graphics and Interactive Techniques*, SIGGRAPH '87, pages 17–24, New York, NY. ACM. 8

Wei, X., Min, J., and Chai, J. (2011). Physically valid statistical models for human motion generation. *ACM Transactions on Graphics*, 30(3):19:1–19:10. 11

Witkin, A. and Kass, M. (1988). Spacetime constraints. In *Proceedings of the 15th Annual Conference on Computer Graphics and Interactive Techniques*, SIGGRAPH '88, pages 159–168, New York, NY. ACM. 11

Yang, P.-F., Laszlo, J., and Singh, K. (2004). Layered dynamic control for interactive character swimming. In *Proceedings of the 2004 ACM SIGGRAPH/EG Symposium on Computer Animation*, SCA '04, pages 39–47, Aire-la-Ville, Switzerland, Switzerland. Eurographics Association. 9, 10, 27

Ye, Y. and Liu, C. K. (2010). Synthesis of responsive motion using a dynamic model. In *Computer Graphics Forum (Proceedings of the Eurographics Conference)*. 11

Yu, J. and Turk, G. (2010). Reconstructing surfaces of particle-based fluids using anisotropic kernels. In *Proceedings of the 2010 ACM SIGGRAPH/EG Symposium on Computer Animation*, SCA '10, pages 217–225, Aire-la-Ville, Switzerland, Switzerland. Eurographics Association. 74

Zhu, Y., Sifakis, E., Teran, J., and Brandt, A. (2010). An efficient multigrid method for the simulation of high-resolution elastic solids. *ACM Transactions on Graphics*, 29(2):16:1–16:18. 19

Zordan, V. B., Celly, B., Chiu, B., and Dilorenzo, P. C. (2006). Breathe easy: Model and control of human respiration for computer animation. *Graphical Models*, 68:113–132. 8